Self-Organization Of Microdischarges In DBD Plasma

A Thesis

Submitted to the Faculty

of

Drexel University

by

Alexandre Chirokov

in partial fulfillment of the

requirements for the degree

of

Master of Science

November 2003

ACKNOWLEDGMENTS

I would like to thank my advisor Dr. Alexander A. Fridman and Dr. Alexander F. Gutsol for their help and support. They have made these past tree years a valuable scientific experience.

I also would like to acknowledge my deepest appreciation to Dr. Jeremy Grace and Dr. Kurt D. Sieber for providing the experimental part of this thesis, much input and interesting discussions.

I am thankful to all great people who thought me during my life. I address special thanks to my friends and collaborators from past and present.

I am very grateful to my relatives and especially to my wife Kamilla Iskenderova for her patience and support.

TABLE OF CONTENTS

LIST OF TABLES

LIST OF FIGURES

ABSTRACT

Self-Organization Of Microdischarges In DBD Plasma.

Alexandre Chirokov

Alexander Fridman, PhD.

Dielectric-barrier discharge, also referred as a silent discharge, combine the ease of atmospheric pressure operation with non-equilibrium plasma conditions suited for many plasma chemical processes. Numbers of interesting industrial applications in addition to the well know ozone generation was found. In particular, it is very effective in plasma treatment of polymer surfaces to promote wettability, printability and adhesion [1, 2]. In air at atmospheric pressure the discharge consist of large number of filaments that can form at regular pattern. Different types of periodic patterns were observed experimentally. Their properties were analyzed in detail. Microdischarge interaction model in dielectric-barrier discharge was proposed in order to explain experimentally observed patterns. Monte-Carlo simulation of microdischarge interaction in discharge gap based on proposed model was developed. Comparison between modeled and experimental patterns was performed by several methods. Effect of different driving voltage on observed patterns was evaluated. Gas phase discharge chemistry was calculated; impact of patterns on chemistry was investigated. For patterns analyze and comparison 2D correlation function of the pattern averaged over the observed space, Voronoi Polyhedron approach as well as two dimensional Fourier transform was used.

CHAPTER 1: INTRODUCTION

The introduction of fast digital computers made possible the numerical modeling of different plasma phenomena, to provide new insight into fundamental processes in various applications and for different types of plasmas. The possibility of using computer modeling of plasma is a great complement to laboratory experiments and analytical results. Computer simulations have been proven very useful in providing understanding of some discharge parameters that are not easily accessible to laboratory measuring devices. Usually computer modeling involves several steps; at first analytical model is developed then experimental measurements used to validate this model, and as the last step detailed computer model is developed.

Many approaches were proposed for simulation of plasma, choose of particular approach depend on type of plasma and simulation goals. For example for low-pressure plasmas particle-in-cell approach proves to be very useful, where motion of each particle in plasma is simulated. In case of atmospheric plasmas fluid plasma models were developed that describe plasma in terms of bulk ions and electrons transport parameters [3].

1.2 Thesis Objective

From engineering point of view, plasma has become very important part of many industrial processes. The main field in which plasma technology is presently applied is electronics, and surface treatments. For example, in addition to ozone generation, the

DBD in air is commonly used in the web conversion industry where it is known commercially as “corona discharge treatment”. It is used to treat polymer surfaces in order to promote wettability, printability and adhesion [1, 2]. This non-equilibrium discharge is especially advantageous for the web conversion industry because it operates at atmospheric pressure and ambient temperature. The use of the so-called “corona treatment” as well as other various surface modification methods for the manufacture of many different types of products on moving webs is extensively described in the literature.

Recently there has been interest in characterizing and understanding the diverse of phenomenon that can be found in atmospheric pressure discharges [13]. The nature of the discharge depends on the gas mixture employed, the dielectric, and the operating conditions. Both diffuse and filamentary discharges are observed at atmospheric pressure and experimental conditions exhibiting ordering or patterning of barrier discharges have been reported [13]. The development of experimental methods, such as imaging techniques, for quantitative characterization of microdischarges (filaments) and associated cooperative phenomena in atmospheric pressure discharges is lacking. Furthermore, theoretical models describing cooperative phenomena in these discharges are not complete.

In this thesis we report an experimental technique that employs the inherent linearity of photostimulable phosphors for quantitative imaging of microdischarges as well as a novel theoretical model describing multi-streamer interactions and cooperative phenomena in the barrier discharges. Experimental and simulated images were compared using three approaches: Voronoi polyhedra, Fourier transform and the radial correlation

function. Multi-streamer interactions leading to short range structuring of microdischarge channels are found.

The dielectric-barrier discharges DBD are essentially non-uniform in most of cases and consist of numerous microdischarges distributed all over the discharge gap (see Figure 4) as more or less organized pattern, which can be seen in Figure 3, Figure 4. Physical nature of the microdischarges is based on formation, propagation and interaction between streamers – local ionization waves usually moving from anode to cathode to meet avalanches propagating in opposite direction.

The streamers are very fast (about 10^8 cm/s) and cover distance between electrodes in extremely short nanoseconds time range. Electrons leave the gap in about 30 ns, while heavy and slowly drifting ions stays in the gap for several microseconds. Deposition of the electrons on the anode's dielectric barrier prevents new avalanches and streamers nearby until cathode and anode are reversed after about 50 microseconds. After the cathode/anode reverse, the deposited negative charge obviously facilitates formation of new avalanches and streamers in the same old spot. As a result, the many-generation-family of streamers is formed, which is macroscopically observed as a micro-discharge.

Taking into account that electrons leave the gap after each single streamer strike much faster than ions, the microdischarge channel is charged in average positively. This positive charge influences the nearby family of streamers, the neighboring microdischarge. The positive charge intensifies electric field in the cathode area of the neighboring microdischarge, and decreases the electric field in the anode area. Avalanche-to-streamer transition depends mostly on near-anode electric field; therefore

the neighboring microdischarges actually prevent and effectively repel each other (see Figure 17). This quazi-repulsion between microdischarges lead to formation of their organized structure in DBD if number of the microdischarges is big enough, and AC frequency is not too low for keeping the bulk channel positively charged in average, and not too high for interference of AC switching with ions still moving to electrodes. This microdischarge pattern self-organization will be discussed below both experimentally and theoretically.

CHAPTER 2: EXPERIMENTAL SETUP AND RESULTS

2.1 Experimental Setup

The parallel plate configuration of the dielectric barrier cell used in this study is shown in Figure 1. The dielectric barrier discharge cell used in this study consists of an aluminum chamber equipped a high voltage electrode assembly and a gas tight Plexiglas lid. The bottom of the 13"×13"×3" aluminum chamber was covered with a 12"×12"×1 mm thick high purity quartz dielectric barrier. The dielectric covered bottom of the chamber served as the ground electrode. The top (high voltage) electrode is a 4"×4" titanium plate. Titanium is used rather than steel because experience has shown that product contamination can occur when ferrous alloys are used as electrodes in such systems. The top electrode has thickness of approximately 6.35 mm. In order to minimize the localization of electric field at the edges of the driven electrode, there are no sharp edges on the top electrode. All eight edges on the top electrode have been smoothed by matching a radius onto the edge. The radius of the edge is 3.175 mm. The high voltage electrode assembly was located inside the aluminum chamber and a high voltage electrical feedthrough in the Plexiglas lid was used to bring power into the chamber. The Plexiglas lid also contained a UV grade high purity quartz optical window. Gas inlet and outlet ports were located on the aluminum chamber at ground potential. To ensure gas purity and humidity control in our equipment, a 1/3 PSI "poppet" valve was installed on the gas outlet.

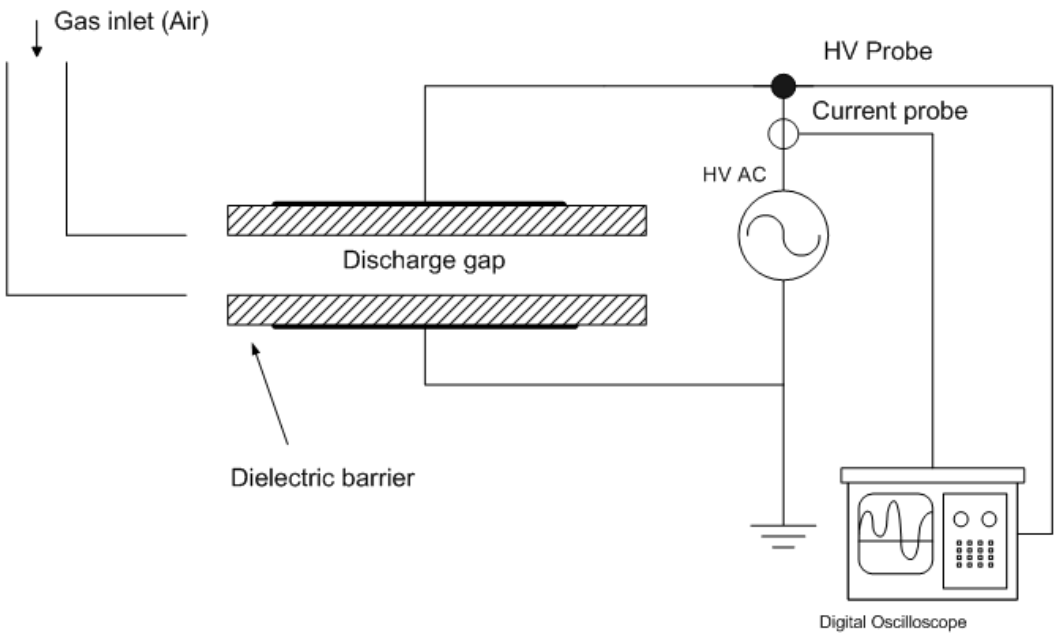

Figure 1: Experimental Setup

The use of the poppet valve allows a small amount of positive pressure to build up inside the cell, thereby minimizing gas diffusion into the cell from the outside. The high voltage electrode was held in a Delrin™ polymer assembly and a low resistance connection between the conducting surface of the high voltage electrode and the high voltage lead was accomplished by means of a spring-loaded electrical contact with the aid of an indium-gallium alloy to wet the conducting surfaces. The high voltage electrodes used in this study was a 5×5 cm area of low resistivity indium tin oxide (ITO) coated on a 1 mm thick high purity quartz substrate. This optically transparent high voltage electrode was mounted in the cell so that the insulating quartz surface of the electrode was facing the discharge gap. The distance between the surfaces facing the discharge gap, (also referred to as the electrode gap), in the cell could be varied between 0.18" and 0.03". The electrode gap setting used in here was 0.06" (0.89 mm). This gap

setting is typical of what is used in dielectric barrier discharges in commercially available web converting equipment.

The gas flow through the cell was controlled using mass flow controllers (Tylan RO-18 electronics with appropriate controllers). Typical flow rates used in this work are around 1 standard liter per minute (slpm). All studies reported here were done in air at ambient temperature. The air to the system was supplied by a laboratory compressor and was filtered and dried before use. The water content of the air was measured on-line using a calibrated Luft infrared analyzer (MSA LIRA) and was determined to be less than 0.3% H_2O on a parts per unit volume basis.

The nominal operating frequency for most of the experiments described here was around 20 kHz. This frequency is typical of the frequencies employed in commercially available power supplies found on web conversion equipment. A Tektronix P6015A high voltage probe and a Pearson current transformer (model 2100) were installed on the high voltage side of the step up transformer. The voltage and current waveforms from the setup were acquired using a high speed digital oscilloscope (Tektronix 544A) and the dissipated power was calculated from the waveforms using either the math functions in the digital oscilloscope or by analyzing the current and voltage waveforms directly by the Lissajous method [14, 15]. Typical steady state power settings employed in the cell and measured on the high voltage (secondary) side of the transformer were between 20 and 150 W.

Both the voltage amplitude and voltage pulse train duration were used to control the exposure of the imaging plate (described below) to the discharge. This was accomplished by the use of two waveform generators. The high frequency waveform

provided by a Wavetek model 29 programmable digital waveform generator was gated by an HP-8111A waveform generator to apply the desired gated waveform to the cell. An ENI model 1140LA power amplifier amplified the gated driving waveform. The output of the power amplifier was stepped up to high voltage using a matching network and a commercially available power transformer (Plasma Technics, Racine WI) then applied to the high voltage electrode of the dielectric barrier discharge cell. The load matching technique employed allowed the cell to be operated in a frequency window between 10 and 25 kHz. The waveform traces observed in our system show evidence of transformer ringing and the circuit resonance appears to limit the lowest achievable time integrated dissipated (secondary) power. When appropriate, the time integrated power per unit area dissipated on the imaging plate was used a metric for comparing images during this study.

The emission spectrum of the discharge was acquired with a grating monochromator using a PAR model 1460 OMA console with a model 1420 intensified diode array detector. The equipment was wavelength and intensity calibrated before use. All spectra were background subtracted and intensity corrected. Further optical characterization of the discharge was accomplished by monitoring the time resolved emission of the discharges using the N_2 380 nm emission line. The optical emission from the discharge was acquired using a fiber optic, passed through a high throughput monochromator and detected by a photomultiplier tube (PMT) (Hamamatsu R928). The time resolution of the PMT and electronics in our measuring system is approximately 1-2 ns. We chose to monitor the 380 nm emission from the $C^3\Pi_u$ level of N_2 for convenience and because the emission lifetime is on the order of 40 ns [16]. The lifetime of a typical

microdischarge is on the order of 1-100 ns [17] and because of the short lifetime of the molecular nitrogen emission from the $C^3\Pi_u$ system it is found that light pulses from individual microdischarges can be detected using this type of setup. The optical signal from the PMT was digitized using a high-speed digital oscilloscope (Tektronix 544a) for further analysis. Optical emission was acquired either from the side of the discharge or in the direction perpendicular to the plane of the discharge through the ITO high voltage electrode. Counting of optical pulses from the discharge was done with the fiber optic viewing the discharge through the high voltage electrode.

The storage phosphor imaging plates used in this study were provided by the Health Imaging Division of Eastman Kodak Company. The imaging plates were identical to commercially available SO-240 general-purpose radiography screens except that the screens were fabricated without a protective overcoat [18]. This was done to increase the sensitivity of the imaging plate for imaging microdischarges. In our investigations the imaging plate was always placed on dielectric covered ground electrode surface. It should be noted that the use of storage phosphor plates requires some care concerning exposure to ambient light. Many fluorescent lamps can expose the plate and cause a background fogging of the plate. A plastic filter over the plate will allow room light handling without causing background on the plate; however, during and after an exposure the plate should be kept in the dark to avoid erasing the photostimulable centers formed in the phosphor. The erasure characteristics of these plates can be found in the literature. The imaging plates were read out using a commercially available storage phosphor reader (Molecular Dynamics Phosphor Imager Model 425 with Molecular Dynamics Image Quant software). The pixel size setting for the phosphor reader was 88×88 microns and the PMT

voltage was the default scanner setting of 800 V. The signal from the plate during scanning was low due to the extremely small amount of energy deposited during some of the experiments; however, adjustment of the linear gray scale range allowed easy visualization of the image. The 8 and 14 bit TIFF files were generated from the scanner for further image analysis using either commercially available or custom written image analysis programs.

A typical microdischarge imaging experiment starts with erasing imaging plate and setting up the cell. The discharge cell is set up by installing the dielectric in the appropriate location in the cell and setting the distance between the imaging plate and the dielectric covered bottom of the high voltage electrode to the desired setting. The imaging plate is placed on the dielectric covered ground electrode, the discharge cell is closed and the gas flow started. The cell is purged until the desired humidity is obtained (0.3%). The lights in the room are turned out and the imaging plate is exposed to the discharge. The secondary voltage and current waveforms are synchronously acquired during the discharge exposure. In many cases, synchronous optical pulse measurements are acquired as well. After the imaging plate is exposed to the discharge, the cell is allowed to purge to remove ozone and oxides of nitrogen then the plate is removed and read out with a storage phosphor reader. After reading the plate is erased and placed back into the cell for the next experiment.

2.2 Imaging of Microdischarges

Various techniques for imaging microdischarges have been described in the literature. One of the oldest methods for imaging microdischarges is the Lichtenberg method [19, 20]. The photographic images generated by this technique are known as Lichtenberg figures. In this method the light emitted from a microdischarge is imaged using a piece of photographic film. The film may be placed underneath a transparent insulator such as glass or quartz to record the plasma optical emission or it may be exposed directly to the discharge. The information obtained from such images includes the physical dimension of the footprint of the microdischarge as well as an estimate about microdischarge density in terms of strikes per unit area. Images of electrostatic phenomena, regardless of how they are generated, are generally referred to as Lichtenberg figures. The work reported here demonstrates the use of imaging plates containing photostimulable phosphor for characterization of dielectric barrier discharges in air through the use of Lichtenberg type figures.

Photostimulable phosphors are also known as “storage” phosphors. This unique class of inorganic materials has the remarkable property of “storing” the energy from ionizing radiation in the form of radiation induced lattice defects whose energy can be liberated by selective photostimulation. The particular material used in this study is the same storage phosphor used for computed radiography applications - europium activated barium fluorobromoiodide. This phosphor crystallizes with the matlockite structure and has the chemical composition of $BaFBr_{1-x}I_x$:Eu (BFBI). BFBI has been studied extensively and optimized for the creation of point defects like F centers upon exposure

to x-radiation. The number of defects created is proportional to the energy exposure or dose. The phosphor is called "photostimulable" because the radiation-induced defects can be "read out" by stimulating the defects with light (photostimulation). In the case of BFBI, irradiation in the F center absorption band promotes defect recombination processes that lead to energy transfer to the Eu^{+2} activator cation resulting in the characteristic blue Eu^{+2} emission. Raster scanning of the exposed imaging plate allows the two dimensional energy pattern on the plate to be digitized. The plate can be "erased" or cleaned of residual photostimulable after reading by flooding the exposed surface with light of the appropriate energy. It is then available for reuse.

Storage phosphors have been applied to a variety of diverse imaging problems. For example, the use of photostimulable storage phosphor plates in radiography is well known and the technique is commonly referred to as computed radiography. Photostimulable phosphor systems are used for imaging synchrotron radiation [21] as well as for neutron detection in neutron diffraction and neutron radiography [22]. Storage phosphor imaging is reported for extreme ultraviolet-vacuum ultraviolet spectrum detection from synchrotron and lasers [23, 24]. Biochemical applications of storage phosphor imaging include the imaging of electrophoretic gels containing radionuclides (including 32P, 14C, and 35S) for DNA characterization studies [25]. The use of storage phosphors to image electron beams in transmission electron microscopy and for electron beam dosimetry has been reported [26]. Storage phosphor screens have been used to image paper formation with beta radiation [27]. We describe here what we believe is the first reported use of storage phosphor imaging plates for microdischarge imaging.

The use of storage phosphor imaging plates offers some advantage over photographic film for imaging microdischarges in barrier discharges. For example, in contrast to the non-linear sensitometric response of photographic emulsions, storage phosphor plates show a wide range linear response with respect to impinging energy. This means that the signal intensity at any particular pixel is directly proportional to the amount of energy deposited. We have verified in our equipment that the signal intensity in the images is linearly proportional to the dissipated power in the barrier discharge cell.

The resolution of a storage phosphor imaging system is limited by the resolution of the imaging plate. In practice the typical pixel size employed in the scanners in between 80 microns × 80 microns up to 170 microns × 170 microns. Although it can be argued that storage phosphor plates are not as high resolution as photographic film, the spatial resolution is sufficient to allow imaging of microdischarges. It is known in the literature that the dimension of the radius of a single microdischarge from a barrier discharge is on the order of 100 microns [13]. Our investigations suggest that even lower resolution images with larger pixel sizes (176×176 micron pixel size) are adequate to characterize the microdischarge spatial distributions. At higher resolution scanner conditions we believe that the storage phosphor method has sufficient sensitivity so that it is capable of imaging single microdischarges. A major advantage of this method is the ease with which digital data files can be generated for further examination with image analysis methods.

The minimum energy for creation of a photostimulable site in the BFBI lattice is determined by the optical absorption edge of the material because the generation of excitons leading to the formation of photostimulable centers is quite efficient near the

optical absorption band edge in these materials. Reflectance measurements of BFBI screens, shown in Figure 2 show decreasing optical absorption at wavelengths longer than 300 nm (approximately 4 eV). The optical absorption edge measured for the screen is not as pronounced as that of the pure phosphor because of additional optical absorptions in the screen attributed to proprietary additives in the screen. For comparison, the optical emission spectra of the atmospheric pressure dielectric barrier discharges investigated in this study are given in the same figure. The discharges show most of their emission at wavelengths between 300 and 450 nm. Although we have not shown the results here, the discharges also have negligible emission intensity between 500 nm and 800 nm. This is an important observation because the stimulation region for the barium fluorohalide photostimulable phosphor, (attributed to F center optical absorption), is located in this spectral window. Significant emission from the discharge in this region would have some effect on the observed sensitivity of the imaging system. The lack of optical emission from the discharge in the region of F center absorption suggests that there is little, if any, signal intensity erasure during plate exposure to the discharge. In addition, there was no evidence of signal saturation during our investigations but we did not extend our work to extremely high power levels. We have not investigated in any depth the stability of pre-existing photostimulable centers in the imaging plate with respect to the extremely large high frequency voltages employed in barrier discharges but the linearity of the signal response with respect to discharge exposure suggests that this effect is not highly significant. Storage phosphor imaging plates can be excited both optically and by electron bombardment. It is important to assess the relative contribution of each type of excitation in the imaging system. The data given in Figure 2 indicates that

there is some optical charging of the storage phosphor plate when the plate is exposed to a barrier discharge in air because of the overlap between the optical emission from the plasma and the optical absorption of the storage phosphor. To determine the contribution of photostimulable centers from the discharge UV emission to the overall image intensity we ran a set of experiments where the position of the imaging plate with respect to the quartz dielectric barrier was changed. In one set of exposures the imaging plate was placed above the quartz dielectric and directly exposed to the discharge. A second set of exposures was done where the imaging plate was located under the quartz dielectric so that only light emitted from the discharge could cause a signal on the imaging plate. The dissipated power, the exposure time, the electrode gap, and the percent water in the atmosphere were held constant during these experiments. Note that the capacitance of the cell was not changed by switching the positions of the dielectric with respect to the imaging plate and therefore any observed changes in the resulting image must be related to differences in the excitation of the imaging plate. Instead of a slight drop in the overall intensity of the image as would be expected if the photostimulated luminescence was due mostly to optical excitation, we found that the overall intensity of the signal read out from the imaging plate when it was located under the dielectric during exposure was about an order of magnitude lower than the signal obtained during readout when the plate was exposed directly to the discharge. We interpret these observations to mean that the formation of photostimulable centers as a result of UV excitation comprises about 10% of the total signal intensity in the image. We conclude that electron bombardment of the phosphor from the microdischarge is the main excitation responsible for the formation of photostimulable centers on the imaging plate.

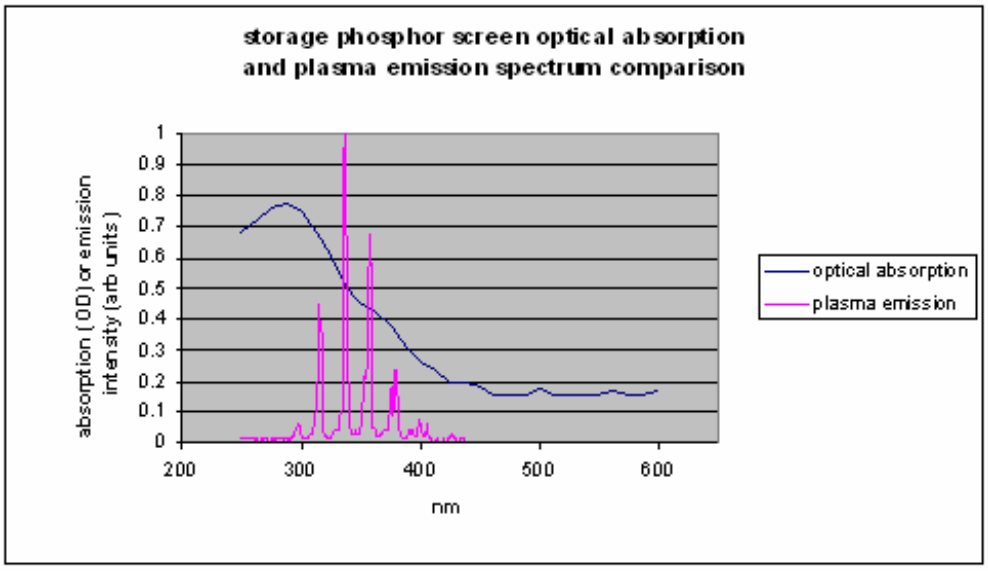

Figure 2: Storage Phosphor screen optical absorption and plasma emission spectrum comparison.

A comparison of optical pulse counting measurements over a known collection angle with features observed in images taken at extremely low dissipated power was used to obtain a very rough estimate of the lower limit of the sensitivity of the imaging system. The Molecular Dynamics storage phosphor reader used in this study has a sensitivity of around 2000 PMT counts per microdischarge feature observed under our scanning conditions. We will ignore the contribution from the UV excitation since our results suggest that it contributes a small amount of the overall excitation. We will assume that between 50% and 60% of the impinging electrons from the microdischarge have an energy greater than 4 eV and that around 10^{10} electrons are passed in the current dissipated in the microdischarges that can be imaged. The higher energy electrons in the microdischarge can, in principle, produce a detectable photostimulable center in the storage phosphor. Although it is unrealistically large, we will take the production efficiency for electron impact formation of photostimulable centers to be equal to 1. The estimated detection efficiency of the system used in this study is between discharge 10^{6}

and 10^7 electrons (roughly 5×10^6 electrons) per 1 detected photostimulated luminescence count from the imaging plate. In fact, the actual production efficiency for formation of a photostimulable center by electron impact is most likely considerably less than 1 and so the sensitivity estimated here probably represents the highest possible sensitivity for the imaging system.

The storage phosphor imaging technique is, in principal, capable of providing an estimate of the electron temperature of the discharge. This measurement requires a characterization of the total amount of dissipated current from the discharge as well as the sensitivity of the imaging system in terms of coulombs per photon of photostimulated emission. A microdischarge in a dielectric barrier discharge in oxygen typically dissipates about 5 microjoules of energy and the total amount of charge transferred is between 0.1 to 1 nanocoulombs [26, 28, 29]. This corresponds to a total number of electrons per microdischarge of between 6×10^9 and 62×10^9, which is similar to our own experimental observations. Taking into account that the imaging microdischarges with storage phosphors uses the higher energy electrons in the microdischarge (since storage phosphors require a minimum energy of around 4 eV for the creation of photostimulable centers), the electron temperature can be estimated as 3-5 eV. The following section presents examples of images obtained by this method.

2.3 Experimental Images of Microdischarges

The Figure 3 shows an 8-bit image of a dielectric barrier discharge in air obtained from the experimental setup. In this experiment the flow rate of air was 5 slpm and the

gap was 0.2" (5 mm). The real discharge area was 5×5 cm. The discharge image presented in Figure 3 was obtained using one applied excitation cycle at 20.4 kHz. Digital oscilloscope traces from the secondary side of the transformer indicate that the high voltage transformer shows some ringing after the initial amplified waveform is applied to the primary side. An examination of synchronous optical pulse counting from the discharge showed that the discharge actually occurred over 1.5 voltage cycles. The microdischarge features in Figure 3 appear to be randomly distributed.

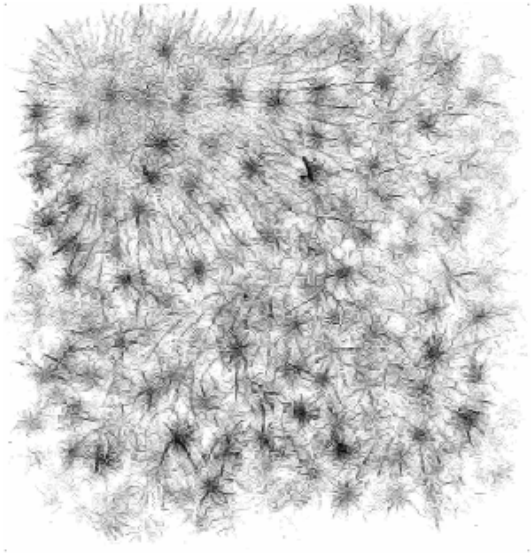

Figure 3: The top-view image of filaments in dielectric barrier discharge gap in air obtained from experimental setup. A storage phosphor screen was placed at the surface of the insulator in the discharge gap.

Figure 4 was obtained using discharge conditions of 10 applied cycles at 20.9 kHz, airflow rate of 1 slpm, and a gap of 0.03 inches. Images taken with applied voltage cycles higher than 5 were all quite similar except that the image intensity increases with increasing discharge exposure time. Note that the images do not show localization of

microdischarge density around the edges of the electrode. This indicates that electric field localization at the electrode edges is not a strong effect under these experimental conditions. The sharper black points correspond to microdischarges that are stationary and occur repeatedly in the same location. We observe that the microdischarges become stationary in our apparatus under these conditions at between 5 and 10 cycles of applied voltage. The localization of the microdischarge position is undesirable from the practical perspective of web treatment and can, in principle, lead to spatially non-uniform surface modification. More importantly, we find that the different discharge conditions such as driving voltage frequency and amplitude result in significantly different microdischarge images.

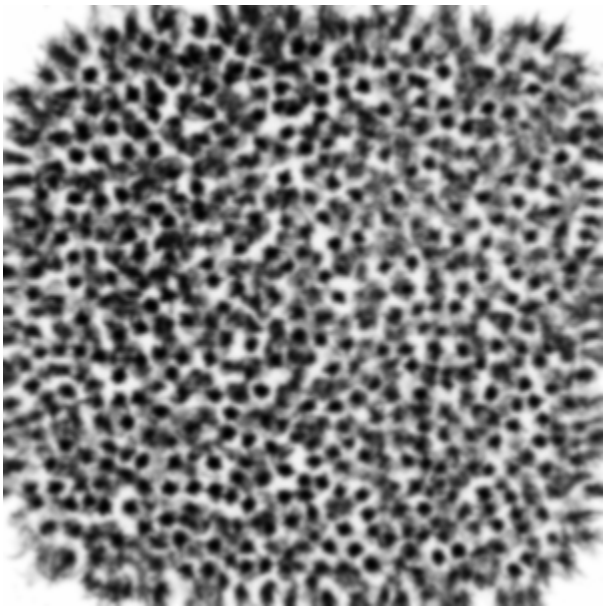

Figure 4: The top-view image of filaments in dielectric barrier discharge gap in air obtained from experimental setup using 10 excitation cycles at 20.9 kHz and a discharge gap of 0.03" (0.762 mm).

CHAPTER 3: MODELING AND SIMULATION OF DIELECTRIC BARRIER DISCHARGE (DBD)

3.1 Filamentary Discharge Mode Description: Concept of Streamer

Many investigations showed that at atmospheric pressure electrical breakdown in planar electrode configuration occurs in a large number of short-lived current filaments referred to as microdischarges. Most of the industrial applications of barrier discharges operate in this filamentary mode [6].

In high electric field electron can absorb enough energy to ionize neutral atoms or molecules, by direct electron collision. The number of electrons produced by one seed electron per unit drift distance is called first Townsend coefficient alpha:

$$\frac{dN}{dx} = \alpha \cdot N$$

Thus total number of electrons produced by one seed electron equal to $\exp(\alpha \cdot d)$. Number of electrons in avalanche grows exponentially with distance traveled by avalanche and with first ionization coefficient that depend on electric field (Figure 5). At atmospheric pressure, due to the high collision rates, a growing electron avalanche can generate appreciable charge density at its tip, already after traveling a short distance. The local electric field due to charge separation resulting from the difference in drift velocities of electrons and ions is superimposed on the applied field Figure 6.

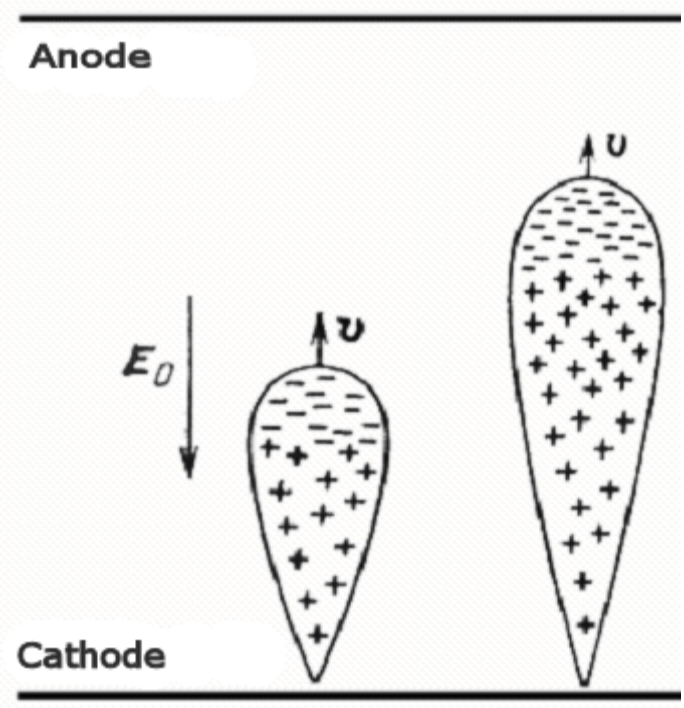

Figure 5: Avalanche propagation.

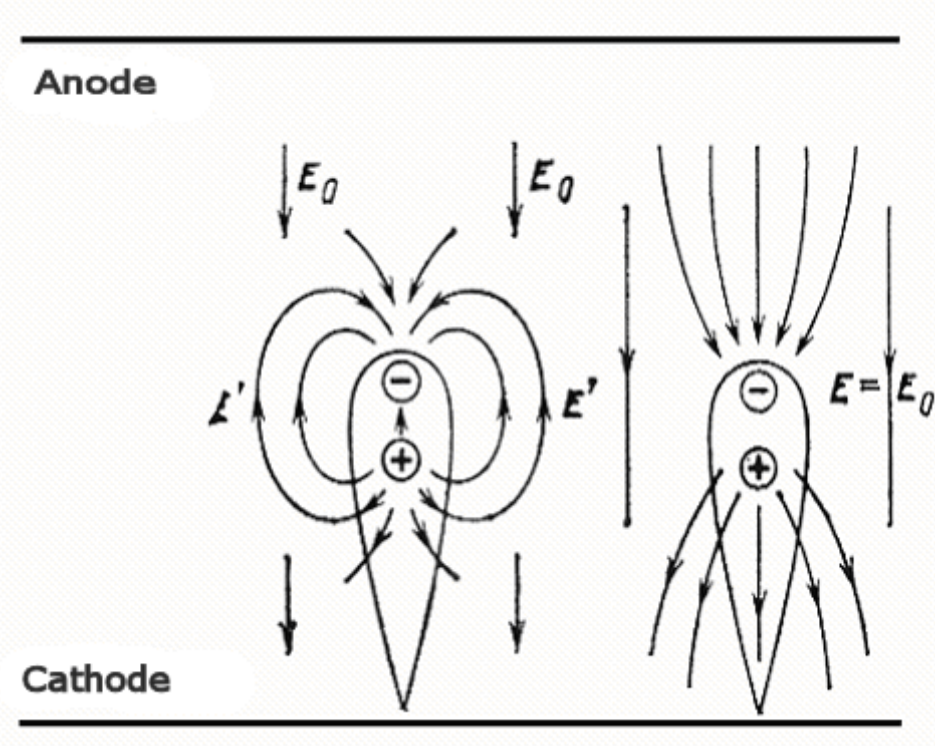

Figure 6: Electric field of avalanche space charge (left), total electric field (right).

Collisional ionization in the high field region at the avalanche head leads to fast propagation of the ionization region and the formation of a bright plasma channel called streamer Figure 7. In air at atmospheric pressure transition to streamer occur when more then 10^8 electrons accumulated in avalanche, which corresponds to $\alpha \cdot d \approx 20$. The streamer velocity is in the range 10^7-10^8 cm/s, the radius of the propagating streamer head and the resulting ionized channel is about 10^{-2}-10^{-1} cm. The reduced field E/N at the streamer head can reach 500 to 800 Td (1 Townsend or Td corresponds to 10^{-17} Vcm^2), a value that is several times higher than the reduced field at breakdown (about 100 to 200 Td). In atmospheric pressure air the thickness of the propagating ionizing region is only 0.02 cm. In the channel electron densities of 10^{14} cm^{-3} and current densities of j ≈ 1000 $mAcm^{-2}$ are reached [9]. Ultraviolet (UV) photoinization of the gas ahead of it is the most likely process to provide seed electrons for the propagating streamer.

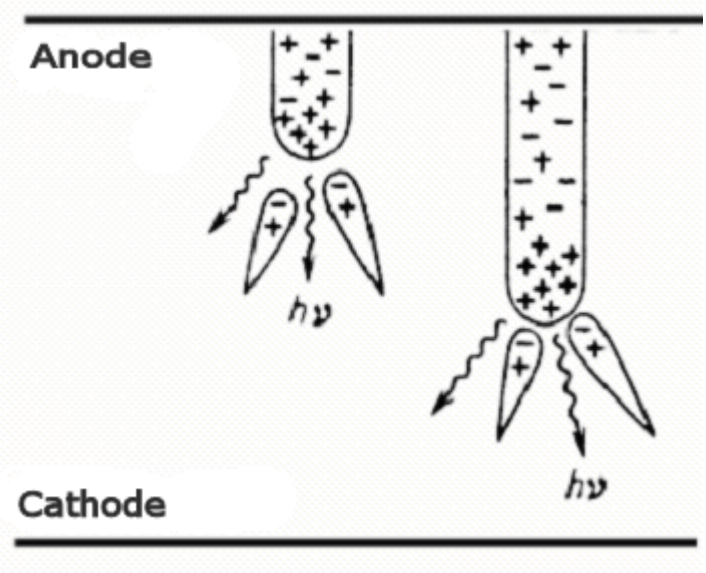

Figure 7: Evolution of the cathode directed streamer.

The early phases of breakdown in a barrier discharge are similar to those without dielectric. In this phase concepts of streamer propagation between metal electrodes as, for example, recently reviewed in detail by Babaeva and Naidis [7], are helpful. Streamer propagation in a given electrode configuration is normally simulated by solving 2D (axisymmetric case) mass conservation equations for neutral and charged particles coupled with Poisson's equation for the determination of the electric field. The equations include inelastic processes, such as ionization by electrons (α), attachment of electrons to oxygen (η), recombination (β) of negatively and positively charged particles as well as photo–ionization (S). The field dependence of the attachment coefficient, ionization and recombination can be described by simple expression as a function of the reduced field E/N [3], see Appendix B.

$$\frac{\partial N_e}{\partial t} = S + \alpha N_e |W_e| - \eta N_e |W_e| - \beta N_e N_p + \nabla(D_e \nabla\ N_e) - \nabla \cdot (W_e N_e)$$
$$\frac{\partial N_p}{\partial t} = S + \alpha N_e |W_e| - \beta N_e N_p - \beta N_n N_p + D_p \nabla^2 N_p - \nabla \cdot (W_p N_p)$$
$$\frac{\partial N_n}{\partial t} = N_e |W_e| - \beta N_n N_p + D_n \nabla^2 N_n - \nabla \cdot (W_n N_n)$$
$$\nabla^2 \varphi = -q(N_p - N_e - N_n)/\varepsilon_0$$

To check certain assumptions, like for example the widely used "local field approximation", assuming electrons in equilibrium with the local field, also more detailed Monte Carlo simulations have been performed. Also simple analytical approximations can yield reasonable results about streamer formation and propagation that agree with numerical 2D models [8].

Table 1: Microdischarge properties in air at atmospheric pressure

Duration:	10-20 ns	Total Charge	10^{-10}-10^{-9} C
Filament radius:	0.1 mm	Electron density	10^{14} -10^{15} 1/cm^3
Peak current:	0.1 A	Mean Electron energy	1-10 eV
Current density	10^6-10^7 A/m^2	Streamer velocity	10^7-10^8 cm/s

3.2 Computer Simulation of Avalanche Propagation: Avalanche to Streamer Transition and Streamer Propagation.

System of equations that describe avalanche and streamer mentioned in previous section is solved using finite element method. Dimensions of the problem are chosen to match those used in experiments. Dielectric barriers (shown in blue) with dielectric permittivity equal to 4 are used on both sides; thickness of one barrier is 0.5 mm, see Figure 8. Discharge gap (space between dielectrics) was 1 mm in height and 1 mm in radial direction, see Figure 8. Cathode is on the top side of domain anode is on the bottom side. Axis of symmetry is on the left side of the domain.

Equation for electric field potential was solved on all three domains, with Dirichlet boundary conditions on electrodes resulting in total voltage applied to gap to be 7 kV. Applied voltage give electric field in the gap 7 kV/1.25 mm = 5.6 kV/mm which is about 200 Td. Equations for density of electrons, positive ions and negative ions were solved only in discharge gap (excluding dielectric domains). We start with 5000 electrons and positive ions distributed according Gauss distribution [3, 8, 7].

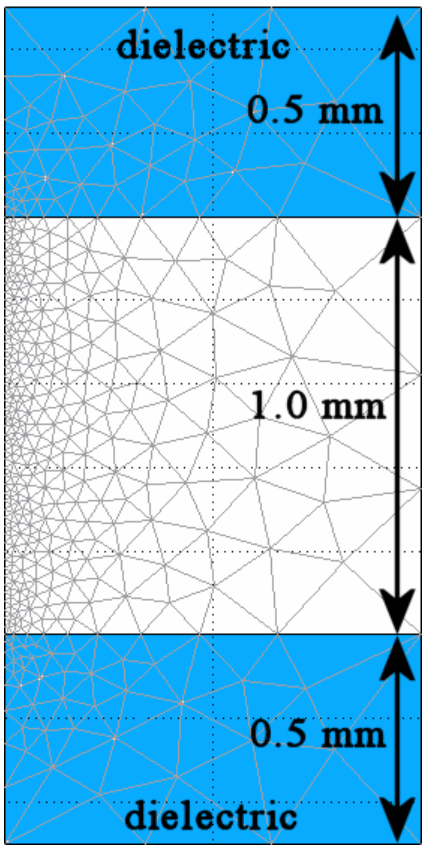

Figure 8: Finite element mesh for streamer simulation, dielectric shown in blue. Top side of domain is cathode while bottom side is anode. Axis of symmetry is on the left side of domain.

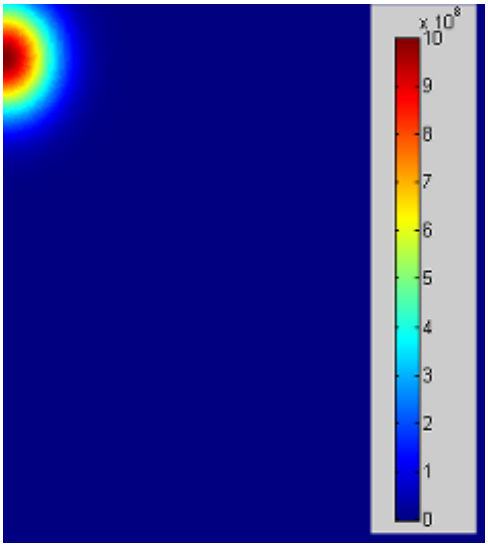

Figure 9: Initial electron and positive ions distribution. Axis of radial symmetry is on the left.

Approximately for the first 1.4 ns electric field of space charge accumulated in avalanche is weak compared to applied electric field (avalanche shape does not change). Number of electrons in avalanche grows exponentially as can be seen from Figure 10. When avalanche accumulate appreciable space charge the electric field in front of avalanche as well as behind is increased. This local electric field increase changes electron drift velocity and makes avalanche propagate faster (avalanche also changes shape at this stage) Figure 11. When avalanche reaches anode the electrons driven by electric field pushed towards dielectric barrier and absorbed by the dielectric surface leaving huge positive charge in the gap, Figure 12. This positive charge can be considered as and extension of anode and thus strongly increases electric field in this region (as would anode have needle like pillar), Figure 13. Strength of this effect depends on charge originally brought by avalanche to the anode which is about $\exp(\alpha \cdot d)$. The size of avalanche which is determined by ambipolar diffusion is also important for the streamer formation. Streamer formation starts at approximately 3.4 ns. Electric field in front of the streamer head can be much higher than applied electric field, Figure 17. In our case streamer has very interesting structure which is hard to see on one-dimensional plots. But one-dimensional plots help to explain very nature of avalanche to streamer transition. Note that majority of publications devoted to streamer formation in large gaps where streamer propagation is not influenced by boundaries. In our case we have different picture. Avalanche moves from cathode to anode started by random electron, and if avalanche brings enough charge on surface of anode streamer might strike back from anode to cathode.

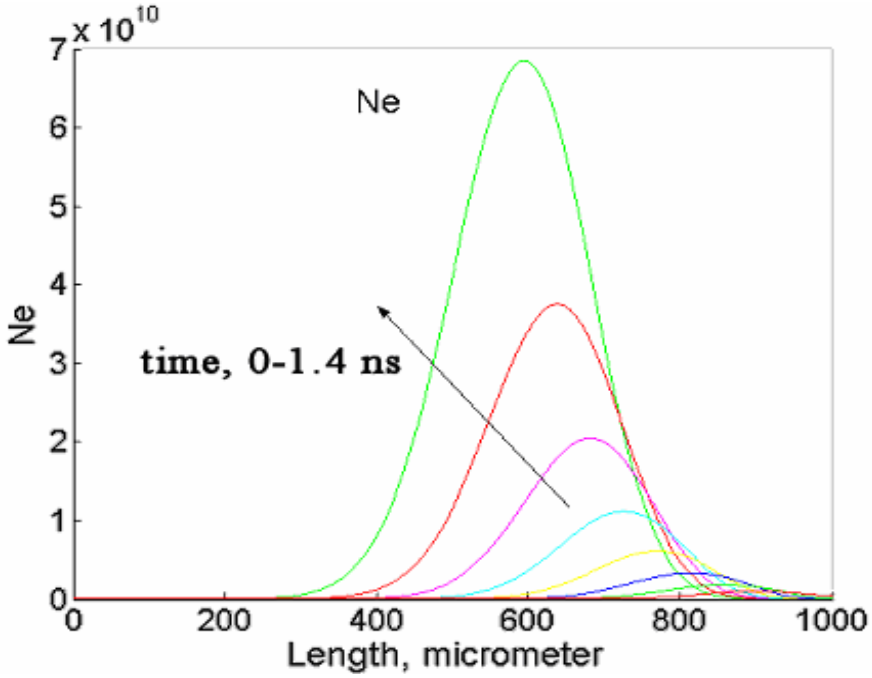

Figure 10: Electron density profile on the axis in avalanche moving towards anode. Time shown from 0 to 1.4 ns. Cathode on right, anode on left.

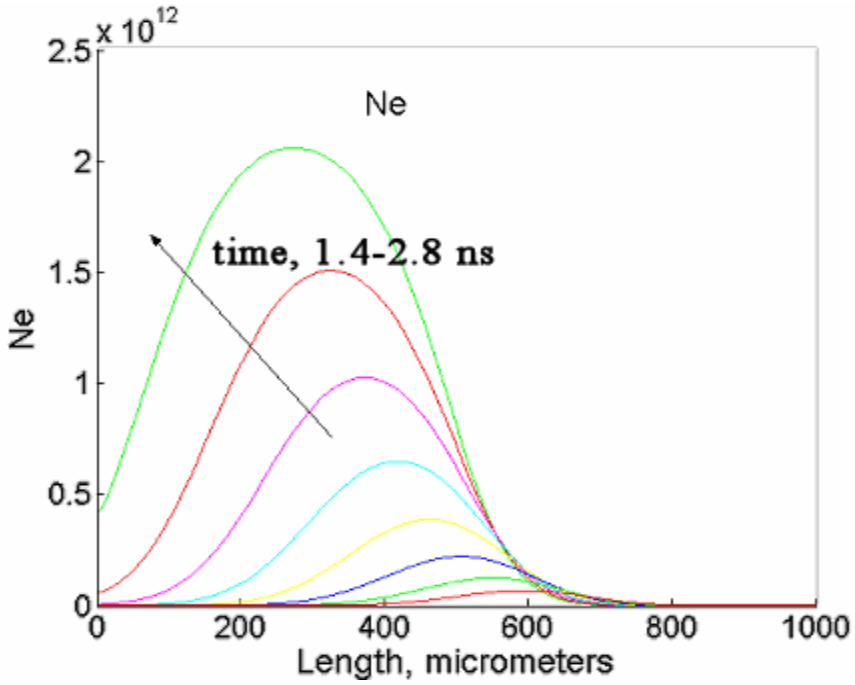

Figure 11: Electron density on axis in avalanche moving towards anode. Time shown from 1.4 to 2.8 ns. Cathode on right, anode on left.

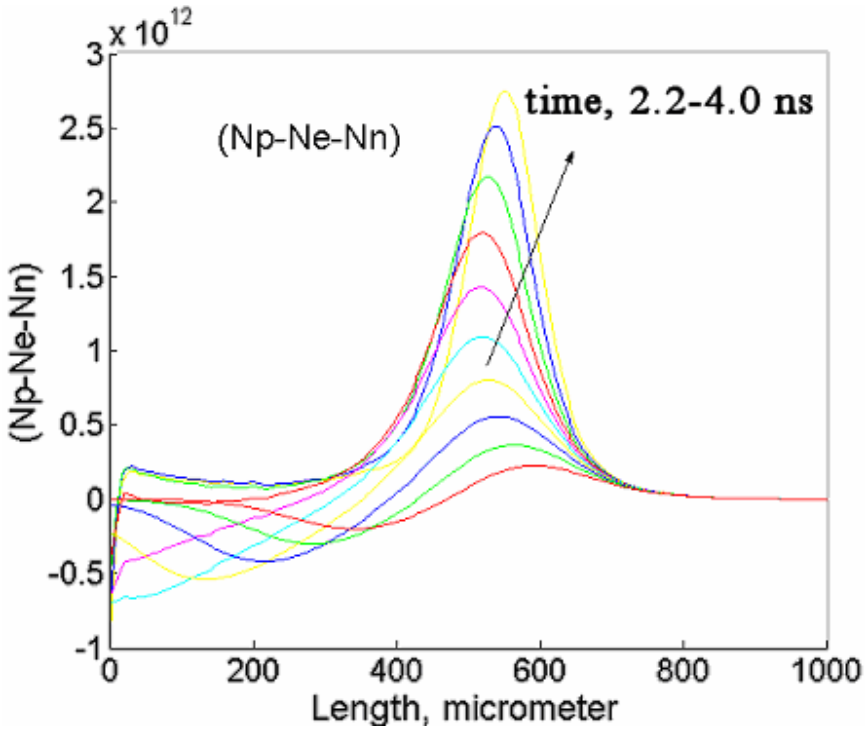

Figure 12: Positive space charge build up, when avalanche reaches anode. Time shown from 2.2 to 4.0 ns.

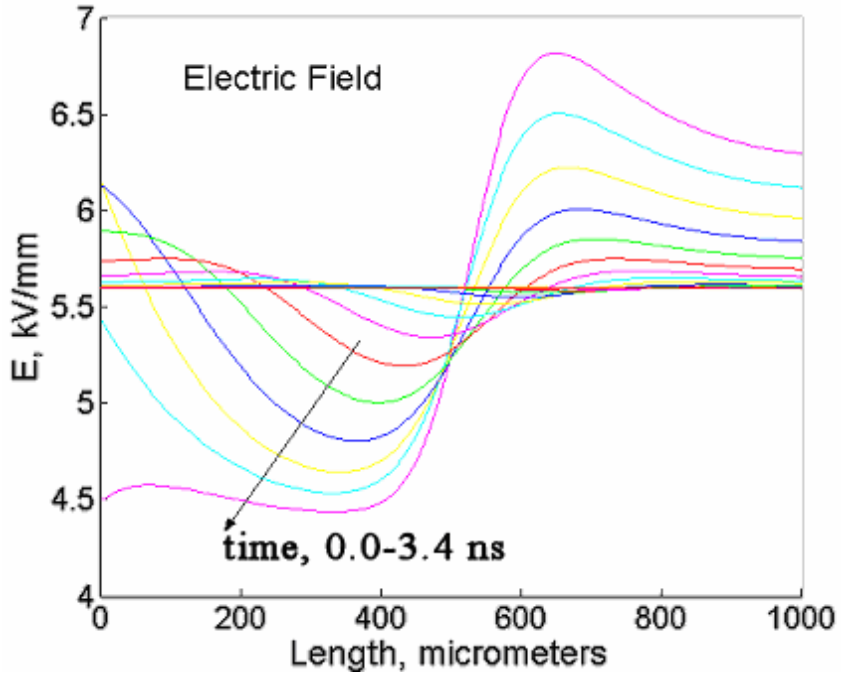

Figure 13: Electric field on axis. Time shown from 0 to 3.4 ns.

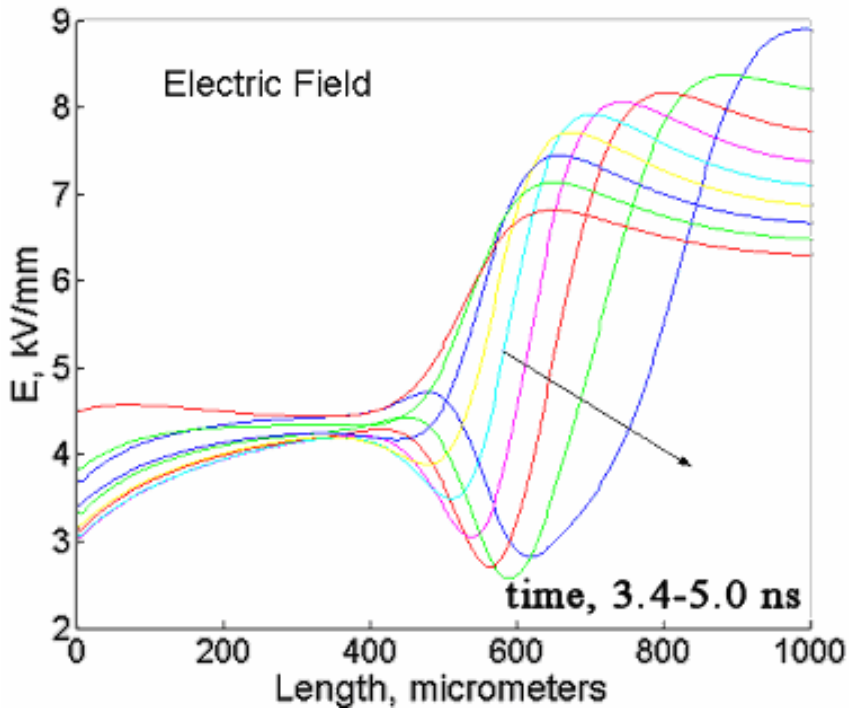

Figure 14: Electric Field on axis. Time shown from 3.4 ns to 5.0 ns. Electric field in front of streamer head is much higher than applied electric field.

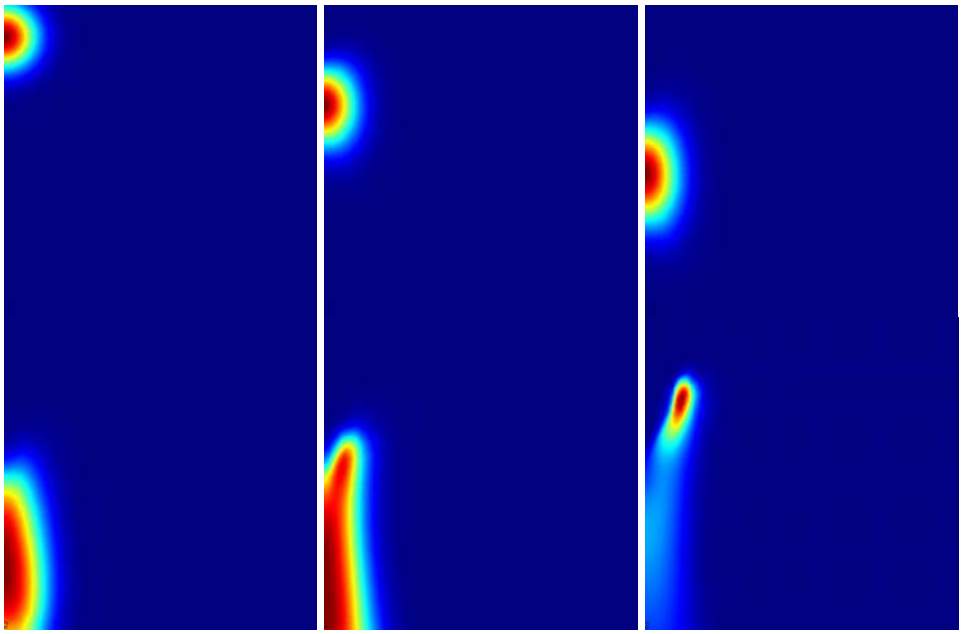

Figure 15: Electron number density. Times shown 0 ns, 1 ns, 2 ns, 3 ns, 4 ns, 4.8 ns. Streamer formation starts at t= 4 ns.

As you can see from Figure 15 streamer in our case has tube-like structure which is impossible to see at one-dimensional plots. For specific values of electron concentration refer to the Figure 11 and Figure 12. Ionization due to streamer results in positive space charge in the gap. Superposition of applied electric field and field due to space charge results in stronger field near cathode and weaker field near the anode, Figure 16. On this figure electric field absolute value plotted on domain boundary of which is 1 mm away from axis of streamer. Streamer space charge has strong effect on electric field even at distant of 1 mm away from the streamer axis (streamer radius is only 0.2 mm). At closer distances effect even stronger. This effect plays significant role in the streamer interaction and will be described in later chapters.

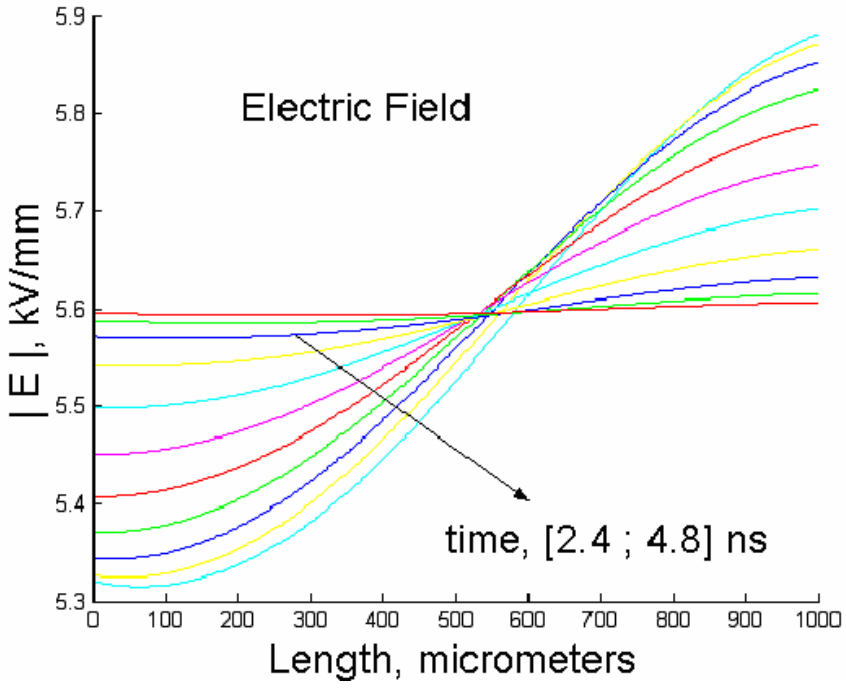

Figure 16: Electric field distortion due to streamer space charge. Anode located at L=0 mm, cathode at L=1 mm.

3.3 Physical Nature of Multi-Streamer Interaction and Microdischarge Structuring: Memory Effect.

At atmospheric pressure discharge occurs in large number of discharge filaments, also called microdischarges. Microdischarge occurs when applied voltage is high enough, that local electric field caused by charge accumulation in avalanches allows streamer formation. Electrons that streamer brings to the surface of anode deposited on dielectric that covers anode. Deposition of the electrons on the anode's dielectric barrier prevents new avalanches and streamers nearby until cathode and anode are reversed after about 50 microseconds. After the cathode/anode reverse, the deposited negative charge obviously facilitates formation of new avalanches and streamers in the same old spot. As a result, the many-generation-family of streamers is formed, which is macroscopically observed as a micro-discharge.

Taking into account that electrons leave the gap after each single streamer propagation much faster than ions, the microdischarge channel is charged in average positively. This positive charge influences the nearby family of streamers, the neighboring microdischarge. The positive charge intensifies electric field in the cathode area of the neighboring microdischarge, and decreases the electric field in the anode area. Avalanche-to-streamer transition depends mostly on near-anode electric field; therefore the neighboring microdischarges actually prevent and effectively repel each other (see Figure 17). This quazi-repulsion between microdischarges lead to formation of their organized structure in DBD if number of the microdischarges is big enough, and AC frequency is not too low for keeping the bulk channel positively charged in average, and not too high for interference of AC switching with ions still moving to electrodes.

Interaction between streamers depends on formation of previous streamers and thus called memory effect. Microdischarge pattern self-organization due to memory effect will be discussed theoretically.

3.4 Multi-Streamer Interaction Model

Microdischarges, or streamers, are the main vehicle of plasma chemical processes in DBDs. The general streamer description is based on the consideration of multiple avalanches formation and propagation. Left side of Figure 17 shows a streamer propagating from the anode to the cathode while attracting additional avalanches. The images shown in Figure 3 and Figure 4 suggest that microdischarges space themselves out.

To begin modeling the phenomena observed in the experimental images we must start by describing the formation of streamers in the DBD. The simplest set of equations containing the basic physics necessary to describe streamer propagation was used [3, 8, 30]. The streamer description used here takes into account gas composition, pressure, power, and current and gives the main characteristics of the streamer.

In this model the actual streamer formation depends only on the local value of the electric field and the discharge gap. To model the interaction between multiple streamers we consider that the space charge field in the microdischarge channel decreases the external applied electric field and prevents streamer formation in the nearby vicinity. The electric field distortion around the streamer as calculated by Poisson's equation is shown in Figure 17. The formation of a streamer at a particular location in the discharge gap also

decreases the average effective voltage drop by where it occurred and consequently prevents formation of subsequent streamers at the same location unless the applied voltage increases also. The point of the discussion is that the streamers will stay separated by a distance corresponding to the length scale of the field inhomogeneity.

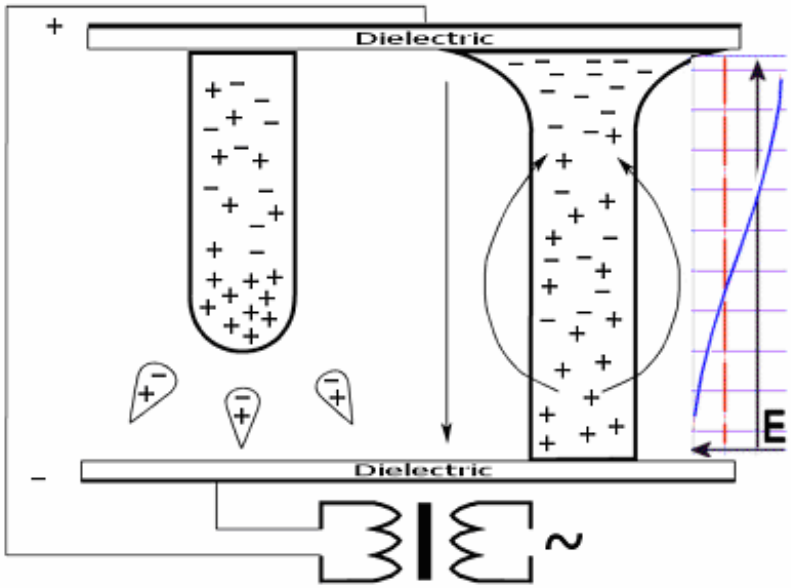

Figure 17: Streamer formation and electric field distortion due to space charge. Blue curve is superposition of electric field of microdischarge and applied electric field; red dashed line is applied electric field. Electric filed is increased at cathode in presence of microdischarge and decreased at the anode.

For given applied voltage amplitude, adjacent microdischarges can get close enough that no additional microdischarges can squeeze between them. If the applied electric field is high enough, it will cause streamers to develop in all the untaken spaces, so that the gap becomes filled from end to end. We consider two types of applied voltage in our analysis of the DBD: unipolar voltage and alternative voltage. In unipolar or DC case (before polarity changes), one of the electrodes remains positive and the other is negative. The streamer always moves in one direction so that another streamer has small

probability to form in the same place until the charge from the first one has dispersed. A different picture appears in case of alternative voltage. There is no need to wait until the charge from the first streamer dissipates. Instead, the probability of appearance of the second streamer in the location of the first streamer increases when the voltage is switched. After the voltage is switched, the electric field of the space charge increases the strength of the applied electric field giving the opportunity for streamer to occur. As a result, the most streamers break in the near vicinity if the previous streamer formed before voltage switching. This describes in simple terms how memory effect in DBD works. The next section presents a Monte-Carlo approach we used to model multiple streamer interactions caused by memory effect.

A probability driven cellular automata (CA) scheme was used in our modeling approach [31]. The cellular automation scheme consists of a lattice of cells that can have any dimensional and size coupled with a set of rules for the state of the cells. At any time a cell can be in only one state. Local rules of transformation from one state to another and the transformation are dependent not only on the initial state of the cell but the state of neighbor cells as well. In this sense the approach employed here is quite similar to the general framework used in many percolation theory calculations. We used a two dimensional stochastic CA scheme. Each cell represents a volume in the gap located between the electrode surfaces as shown in Figure 18. The upper and lower surfaces of each cell are bounded by the dielectric surfaces of the electrodes themselves and the height of each cell is defined by the gap distance. Thus, we define $S_{i,j}$ as an array of states of the cellular automata that can change with time. The value of the time step in the simulation is important and is defined by the variable *dt*. We used the extended form of

CA in which not only the discrete states of CA but also some data about real physical values (charge density, electric field, energy release, random fluctuations, etc) are kept in each cell. CA transformation rules define a new state for a cell during a given time step using not only data concerning the states of all the cells in the CA but also external information such as driving voltages imposed upon the system as a whole. It was assumed that the probability for the occurrence of the next streamer depends only on the local value of the electric field. The position of a microdischarge strike is determined using a Monte-Carlo decision for given probability values in each cell. Since streamers can appear randomly in time as well as in space, an additional Monte Carlo simulation was used to decide whether a streamer will occur or not and Figure 19 shows the flow chart for this procedure.

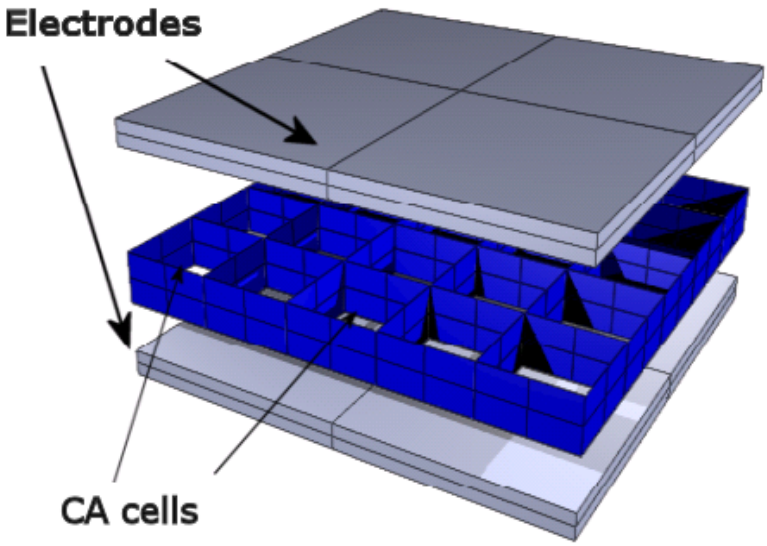

Figure 18: Each CA cell represents a volume in the gap located between the electrode surfaces (shown in gray), cell boundaries shown in blue.

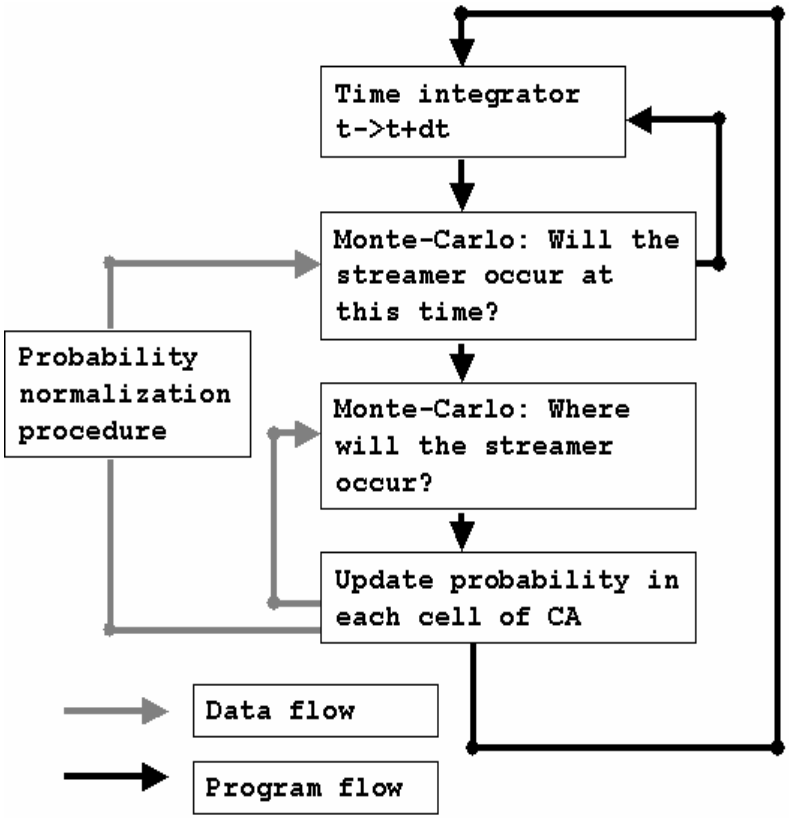

Figure 19: Flow chart for the space and time coupled Monte Carlo simulation

3.5 Simulation Results of Multi-Streamer Interaction Model

The simulation code was developed in C++ and works with arbitrary voltage waveform. The input parameters to the program are the simulation time (number of periods with period length given for the case of AC voltage), driving voltage waveform, size of CA (simulation lattice size), and geometry of the discharge gap. The charge transferred by the streamer is not specified as an input parameter instead it dynamically calculated during simulation based on local electric field strength. The charge transferred by individual streamer decreases the electric field inside the microdischarge channel because it creates a local electric field opposing the external applied electric field. We

assume that the total charge transferred by the streamer is the amount of charge that decreases the local electric field to zero (in other words, electric current through the channel exists until the electric field becomes shielded by space charge). The probability of a streamer striking is calculated from the local electric field by the following formula

$$P(E) = 1 - \frac{1}{1 + \exp(S \cdot \frac{E - E_0}{E_0})}$$

where E is the electric field in the cell, E_0 is the critical electric field necessary for streamer formation given by the Meek condition, and S is ability of the discharge to accumulate memory about previous streamers. In case of large S, the memory effect has negligible effect on operation of DBD, thus the probability function will be a step function that represents the Meek condition for streamer formation. In case of small S, the *memory effect* significantly affects probability of streamer formation. Streamers can be formed in weaker electric fields than required by the Meek criteria in the presence of ions, metastables, and vibrationally exited molecules in the gap and eclectic charge deposited on dielectric surfaces. Value of S represents the cumulative *memory effect* and should be determined from the experiment. We used experimental data from the literature [32] to estimate value S for our system. High operation frequencies tend to decrease value of S as well as other factors that increase memory effect. The output parameters from the program are representative of the density map of streamer activity on the surface of the photostimulable phosphor imaging plate or web. For given voltage waveform the model can calculate the dependence of current on time. A typical result for a simulation over 20 discharge excitation cycles is shown in Figure 20. This particular simulation was performed on with a 50×50 lattice where the DBD cell is driven by a 20.5 kHz sinusoidal

voltage with a 4.5 kV amplitude. The gray scale intensity at any particular cell is proportional to the number of streamers striking the cell. The simulation shows that the streamers occurrence across the simulation lattice is non-uniform: some regions are well treated by streamers and some are not treated at all. This non-uniformity is the result of interactions between streamers and fully developed microdischarges so called Multi-Streamer interaction. The simulation images show good qualitative agreement with the experimental storage phosphor images.

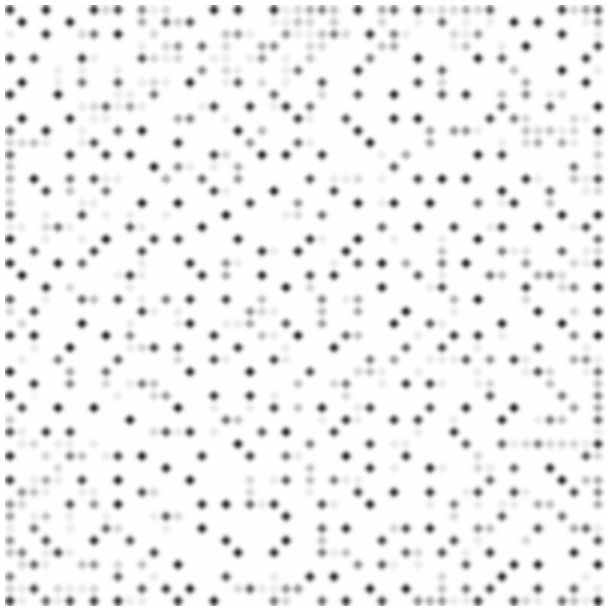

Figure 20: Simulation result on CA size 50×50. This matrix represents the number of streamers strike recorded in CA. Total number of streamers recorded is 17462.

Figure 21: Simulation image of Figure 20 with added noise for visual comparison with experimental images.

The present model is capable not only of simulating the working regime of a DBD system but also can simulate DBD starts. At the initiation of the discharge there is no space charge capable of supporting the streamer formation. During the first period only limited amount of streamers will appear. When space charge starts to accumulate in discharge gap, the number of streamers strikes per period will increase until it reaches saturation level. The time needed to reach saturation level in our model is equal to about of twelve periods. This is shown in Figure 22. This result is in good agreement with the experimental results where it was found that the microdischarges become stationary (full saturated) at between 5 and 10 periods.

Our streamer model does not consider simultaneously developed streamers, but the time between successive streamers could be very small; however, the time step is an adjustable parameter in our model. We tried different values for the time step in the model and found that 1 ns is sufficient to represent various observed time intervals

between streamers. Accordingly, we set the value of the time step (*dt* in Figure 19) to a value of 1 ns. The simulation model allows us to count the total number of streamers occurring under a given set of conditions. Each streamer that occurs can be assigned an index number indicating its order of appearance. In Figure 23 the calculated time interval between subsequent streamers is plotted as a function of index number for one quarter of a period (shaded area on voltage plot). The plot shows that as the applied sinusoidal voltage approaches its maximum value the time interval between streamers increases. The physical meaning of this result is that once a streamer occurs the applied voltage must increase some amount before another streamer will form. This can explained from considering electrical circuit equivalent of the discharge cell. Total capacitance of dielectric barrier discharge will be capacitance of all cells connected in parallel. Parallel capacitors have total capacitance equal to sum of all capacitances. Shielding that occurs in cells due to space charge and charge deposited on dielectric surfaces increases capacitance of cell and thus capacitance of whole system. Increase of capacitance cause voltage drop. Therefore, the average time interval between successive streamers is related to the derivative of the voltage.

By analysis of the optical pulse and secondary voltage waveforms from the experimental DBD cell it is possible to determine the time interval between successive optical pulses resulting from either single or multiple streamers occurring in the field of view of the fiber optics mounted on the cell. Figure 24 shows the experimentally determined time interval between optical pulses for an experimental setup where the discharge gap is 0.06 inches with an air flow of 1 slpm. The data in the figure were accumulated over 6 half cycles and show that the average time interval between optical

pulses is between 0.4 and 0.5 microseconds. The results are not strictly comparable with the simulation results because an optical pulse can contain contributions from multiple streamers occurring within a short time period.

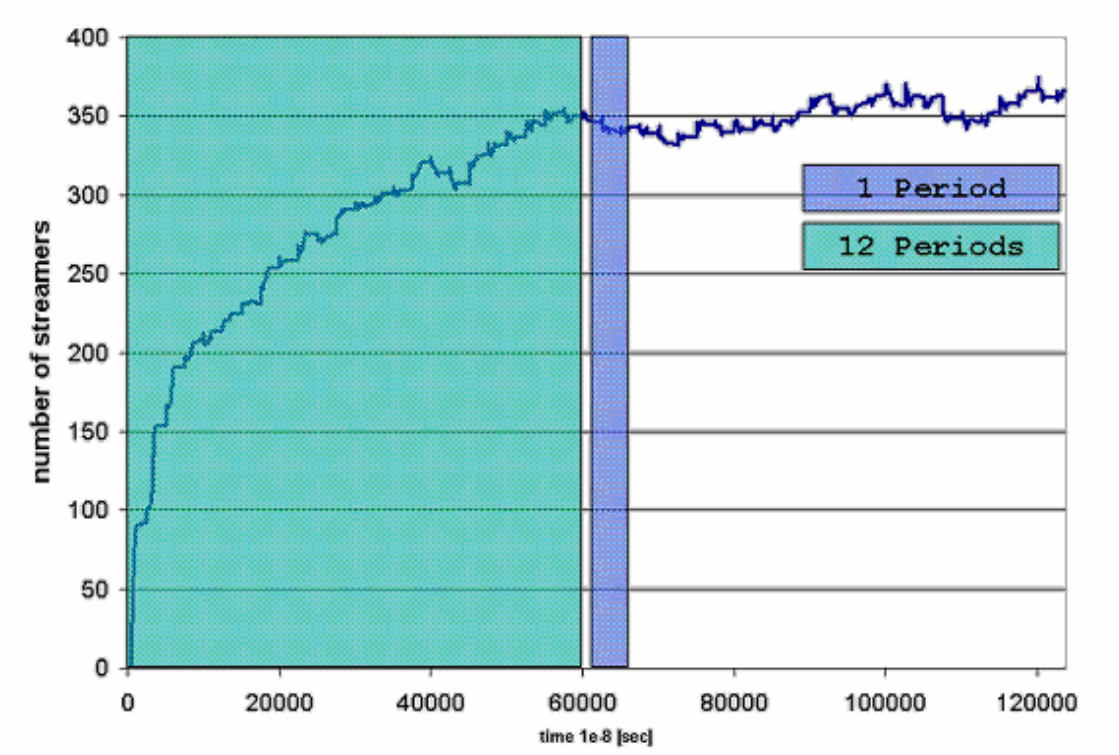

Figure 22: Simulation results showing the total number of streamer channels in the discharge gap with respect to time

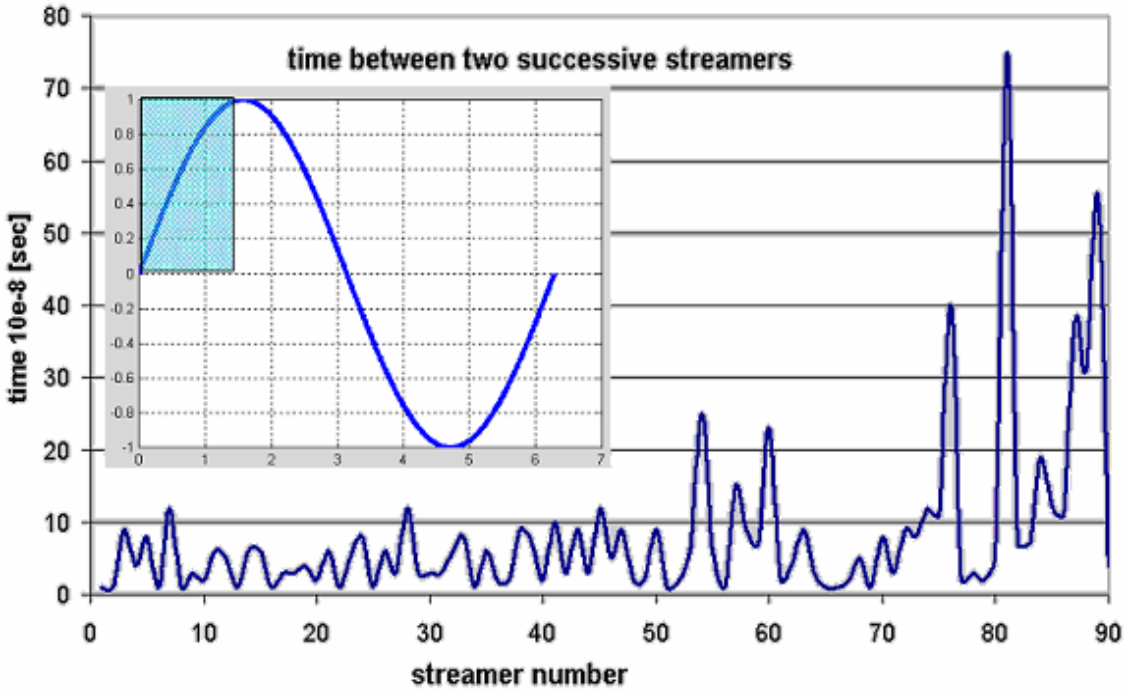

Figure 23: Simulation results showing the time interval between successive streamers during quarter of period (shaded area on the voltage plot).

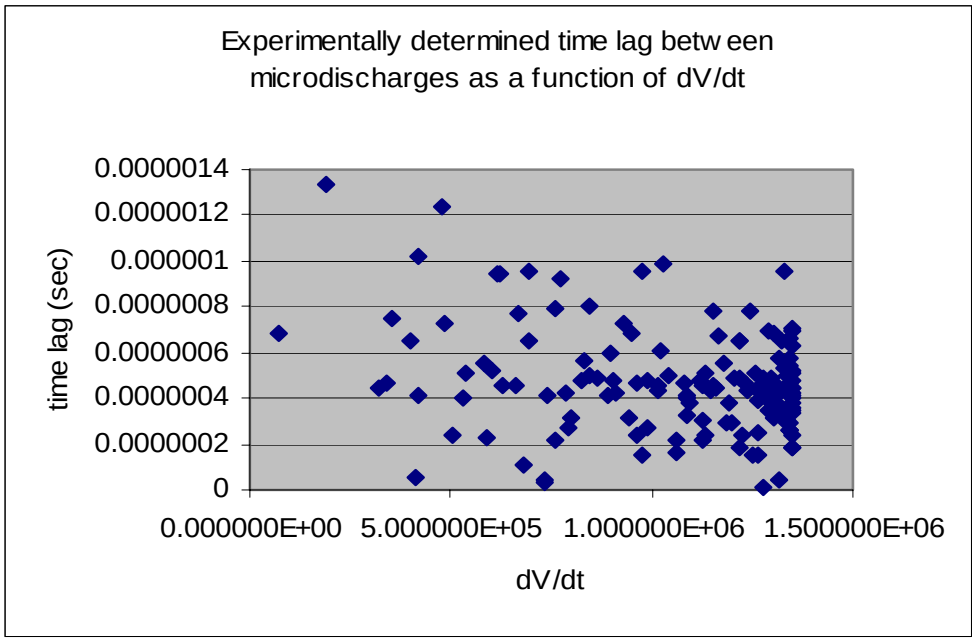

Figure 24: Experimentally determined time interval between optical pulses as a function of the secondary voltage derivative

3.6 Comparative Analysis of Experimental and Simulated Patterns

Our experimental results are in the form of images and our theoretical results can also be expressed in terms of simulated images. Here we present the results of some image analysis used to compare the experimental results with simulated images derived from our probabilistic models. There are many possible methods that could be employed for this purpose. We used two different image analyses: the 2D correlation function [33] and Voronoi Polyhedron approach [34]. Voronoi polyhedra analysis was performed using MatLab software. This analysis defines cells (not to be confused with CA cells, although some CA makes use of Voronoi cells) around selected points in an image. In our images the selected points correspond to microdischarges. Constructing Voronoi polyhedra allow extracting different data from microdischarge image. For example one can use topological date like number of angles in each Voronoi cell and number of edges in each Voronoi vortex or metric data such as area of the cell perimeter of the cell boundaries and sphericity coefficient of cell. Definition of sphericity coefficient rely on the fact that sphere encloses maximum volume for given surface area. In our case we can define two-dimensional sphericity coefficient (c-coefficient) using similar approach. In case of circle c-coefficient equals to one, while for all other shapes will be less than one (maximum c coefficients for hexagon $C_6 \cong 0.9069$, quadrangle $C_4 \cong 0.7854$, triangle $C_3 \cong 0.6046$).

$$\mathbf{C = 4\pi \cdot \frac{S}{L^2}}$$

where S-surface area of cell, L-perimeter of cell

Table 2: Chi-Square (χ^2) test for Voronoi cell C-distribution.

	χ^2	Probability	Critical χ^2(5%)	Similarity
Exper. vs. Simul.	58.2412	0.3570	73.3115	Strong
Simul. vs. Random	207.5134	0.0	55.7585	Negligible
Exper. vs. Ransom	254.2565	0.0	55.7585	Negligible

Table 3: Kolmogorov-Smirnov test for Voronoi cell C-distribution.

	Similarity significance level	Difference
Experimental vs. Simulation	3.37 %	0.1092
Simulation vs. Random	5.4473×10^{-33} %	0.4859
Experimental vs. Random	1.3737×10^{-41} %	0.5343

Voronoi Polyhedra analysis of experimental data (Figure 28) shows that most of the cells in pattern have six angles. The same result we have for the image obtained during simulation (Figure 27). A random pattern of dots on a grid was generated for comparison with the experimental and simulated images using MatLab. The random dot pattern simulated a streamer pattern in the absence of Multi-Streamer interactions. The comparison of the simulated and experimental results with random dot distribution (Figure 30) shows that the distribution of the experimentally obtained pattern looks very similar to simulated pattern, but not to the random one.

In Figure 25 distribution of Voronoi cell sphericity coefficient (c-distribution) is presented. Distribution drawn from experimental data has visually very similar characteristics with one that was constructed from simulation results. In order to provide more elaborate comparison Chi-Square (χ^2) test was performed in order to compare these distributions. Usual acceptance level for χ^2 is based on probability $P = 0.05$ which give us

critical χ^2 value (for given degree of freedom). Chi-Square analysis results shown in Table 2. As you can see from this table there is significant level of similarities with experimental data and no similarity at all with random data. Another method used to test similarities between distributions is Kolmogorov-Smirnov analysis. Result of this test summarized in Table 3 and Figure 26. This method as well as Chi-Square reveals significant similarity between simulation and experimental data. Random distribution (uniform in our case) does not have any similarities with experimental as well as with simulation data, this indicates that streamers do in fact interact with each other (they do not strike randomly!); such interaction we call Multi-Streamer interaction to emphasize cooperative nature of this phenomenon. One of the important conclusions of this is that Multi-Streamer interaction leads to pattern formation in dielectric barrier discharge. How patterns formation affect chemistry in DBD will be described in next chapters.

The correlation function, which is widely used for post processing in crystallography, gives us an idea about an order in pattern, for example, if one can construct the correlation function of gas as a material where the position of centers are random, it would looks like in Figure 36(c), so the function would not have a periodic oscillations. The correlation function for the liquids with the local forces looks like in Figure 36(a), the oscillations exists only at the beginning, because there is no long-range order. For ideal crystal, this function has the oscillations up to infinity, Figure 36(b). From experiment the pattern behaves as a liquid (Figure 36(a)) and the oscillations are smoothed by the noise. In simulation obtained image (Figure 36(b)) the oscillations are more pronounced but have the same liquid characteristic. From the above facts one can

conclude that the DBD pattern is of liquid type and this statement validates by experiment and modeling.

Two-dimensional Fourier transform was computed on the simulated pattern with added noise (Figure 20) to make a fair comparison with experimental one. The power spectrum images (Figure 31) of both experimental and simulated image are similar and have a “donut” in the center. The power spectrum image of random distribution is totally differing from experimental and simulated ones. “Donut” in power spectrum means a local order caused by streamer interactions [38]. Donut in experimental power spectrum is bigger because of the noise presence. Fourier transform was computed using FFTW library (see Appendix C).

To illustrate Fourier Transform ability to detect order in images, consider images in Figure 32. For more details on Fourier Transform ability to extract order see reference [38]. First test image filled with random points (coordinates of each point are random numbers with uniform distribution), corresponding Fourier image have “cloud” in the center of the image. Cloud appears in the center of Fourier image because the distances between points are random and there is no selected frequency. On second test image, we present 2D random pairs; distance between points in pair is constant, the pairs distributed randomly on the image. As you can see from Fourier corresponding image, there is a selected frequency corresponding to distance between pairs. The same effect can be seen on third test picture. High order detection can be as well performed by means of FFT; example of such detection can be seen in Figure 33 and Figure 34.

In Figure 35 the results of order detection in DBD images presented. First image (from left) corresponds to three activation cycles, no pattern was detected by Fourier

transform, and visually it appears that streamers mostly strike randomly. Pattern changes dramatically on the second image. This image was exposed for 60 excitation cycles in exactly the same conditions as was first one. Strong low-order pattern was detected by Fourier transform on second image. The same low-order pattern can be seen on third image as well (exposed by 100 excitation cycles).

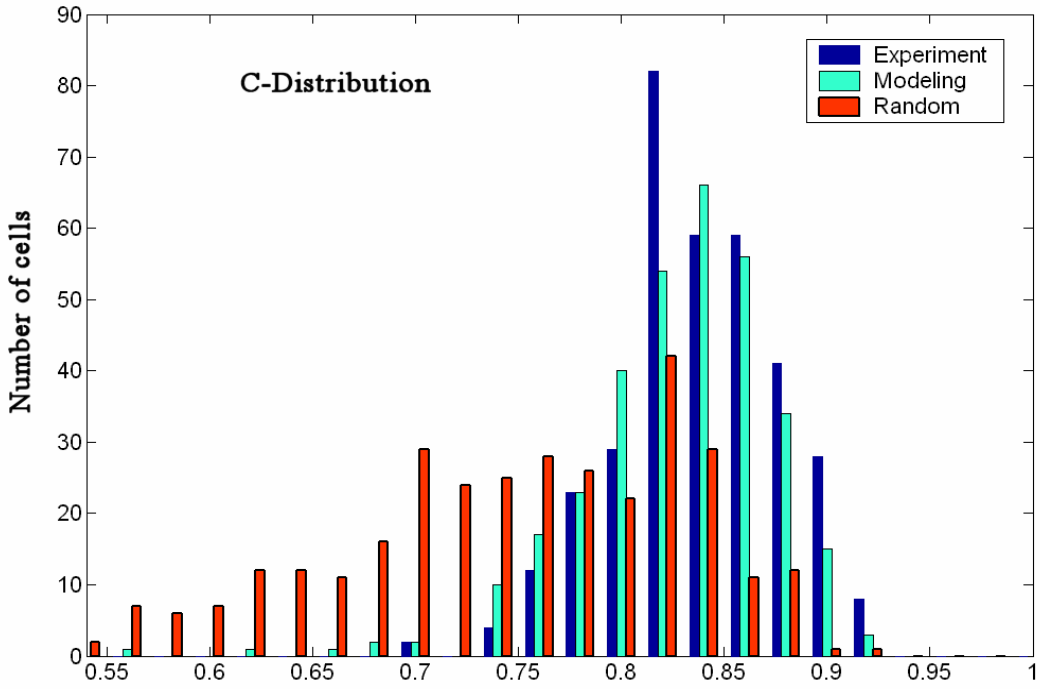

Figure 25: Distribution of Voronoi-cell sphericity coefficients. The experimental data (Figure 28), simulation data (Figure 27) and data from random-point distribution are shown for comparison.

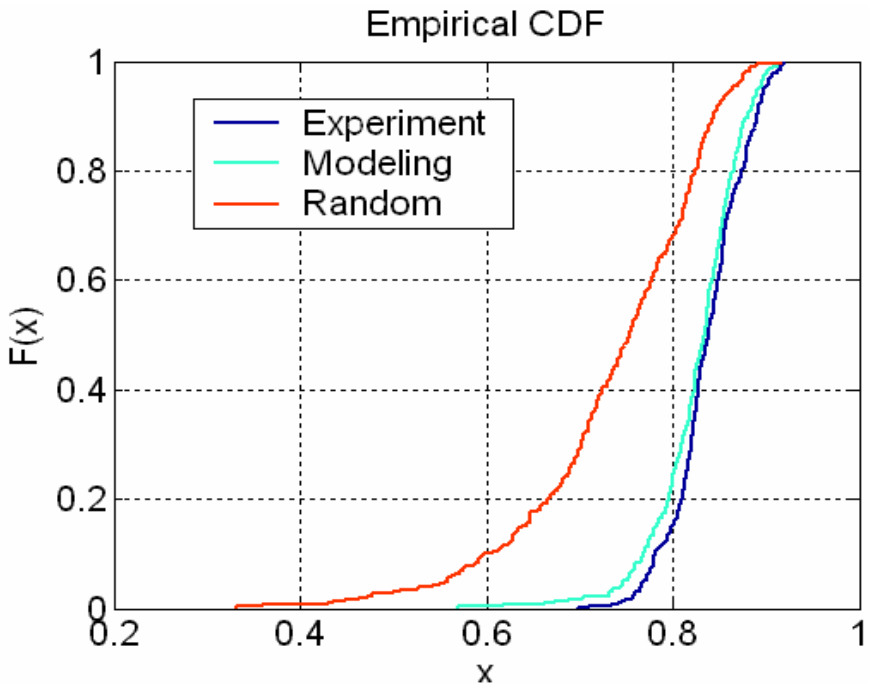

Figure 26: Cumulative Distribution of Voronoi-cell sphericity coefficients. The experimental data (Figure 15), simulation data (Figure 14) and data from random-point distribution are shown for comparison.

Fourier analysis of DBD images shows that for the first few excitation cycles Multi-Streamer interaction does not affect streamers strike probability as no memory accumulated yet in dielectric cell. Images exposed for many excitation cycles show distinct short-distance pattern. Situation does not change much with increasing number of cycles, the same short-order pattern observed. It is clear indication that memory reaches saturation after several excitation cycles. The same behavior of memory effect was observed during simulation, see Figure 22.

First attempt in modeling of DBD memory effect and Multi-Streamer interaction was made. The memory effect and Multi-Streamer interaction result in a streamers pattern formation. The comparative analysis made above verified the validation of our

model of Multi-Streamer interaction, and this model is ready for the further investigations.

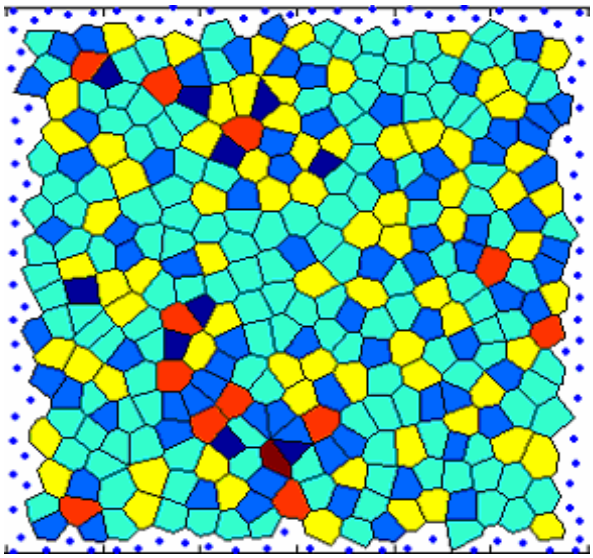

Figure 27: Voronoi Polyhedra analysis of the simulated microdischarge locations from image shown in Figure 20. Polyhedra cells are angle colored. The cells on the image obtained in simulation are mainly six-sides cells.

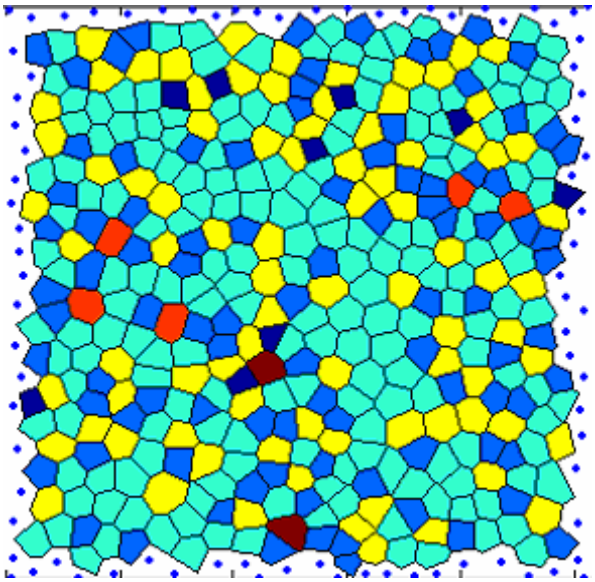

Figure 28: Voronoi Polyhedra analysis of the experimentally obtained microdischarge locations from image shown in Figure 4. The cells on the image obtained experimentally are mainly six-sides cells.

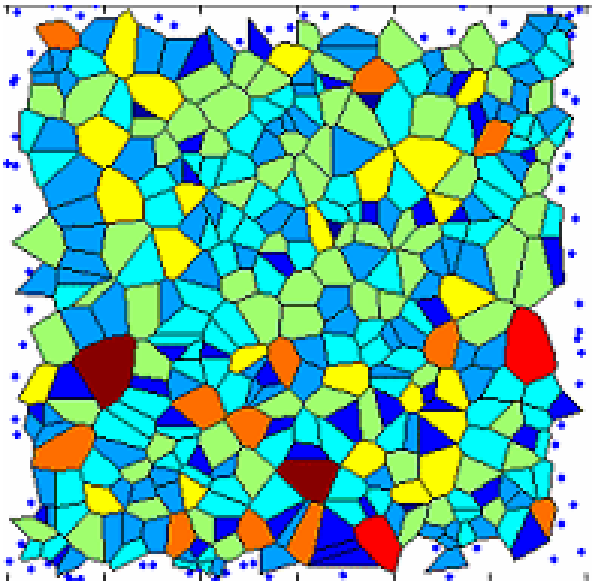

Figure 29: Voronoi Polyhedra analysis of the random streamer strike pattern; shown here for comparison.

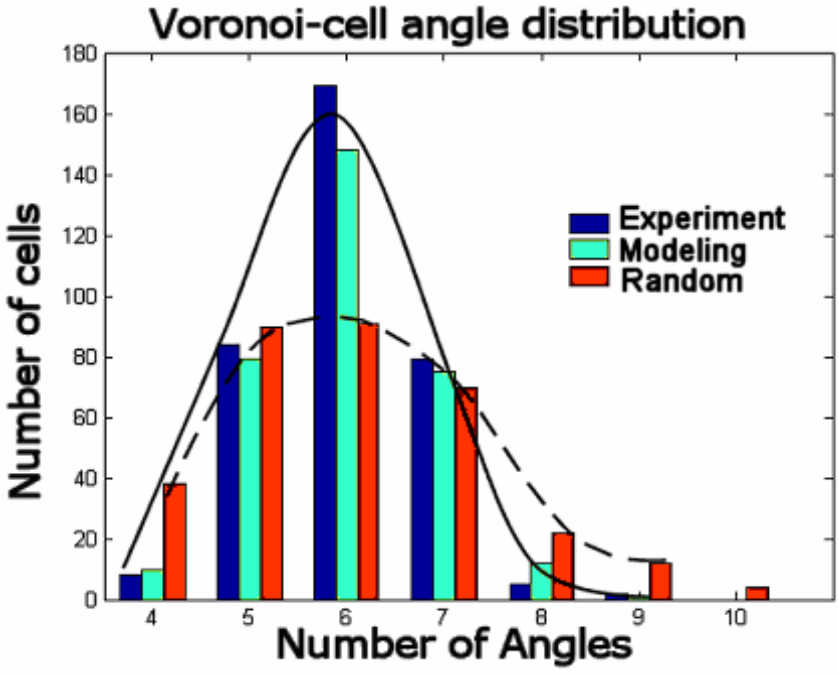

Figure 30: Distribution of Voronoi-cell angles. The experimental data (Figure 28), simulation data (Figure 27) and data from random-point distribution are shown for comparison.

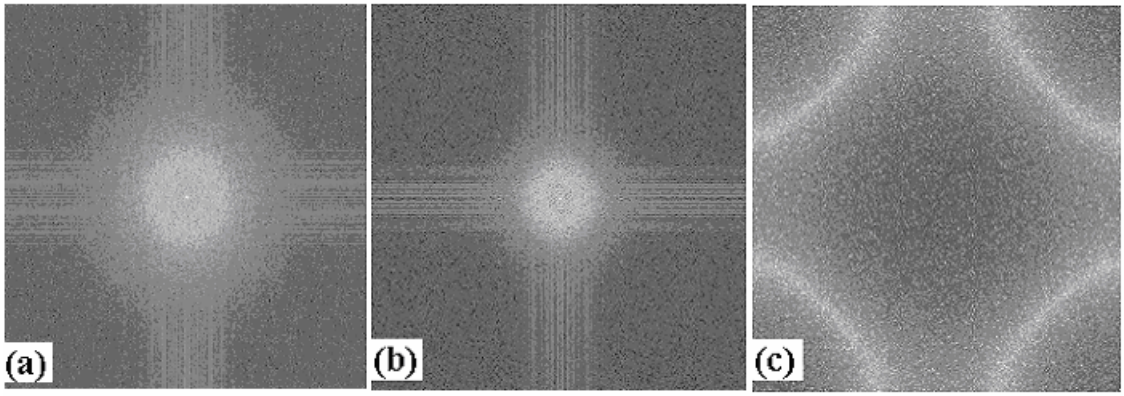

Figure 31: 2D Fourier transforms: (a) of experimental data from image in Figure 4; (b) of simulation data from Figure 20; (c) of data from random-point distribution (shown for comparison).

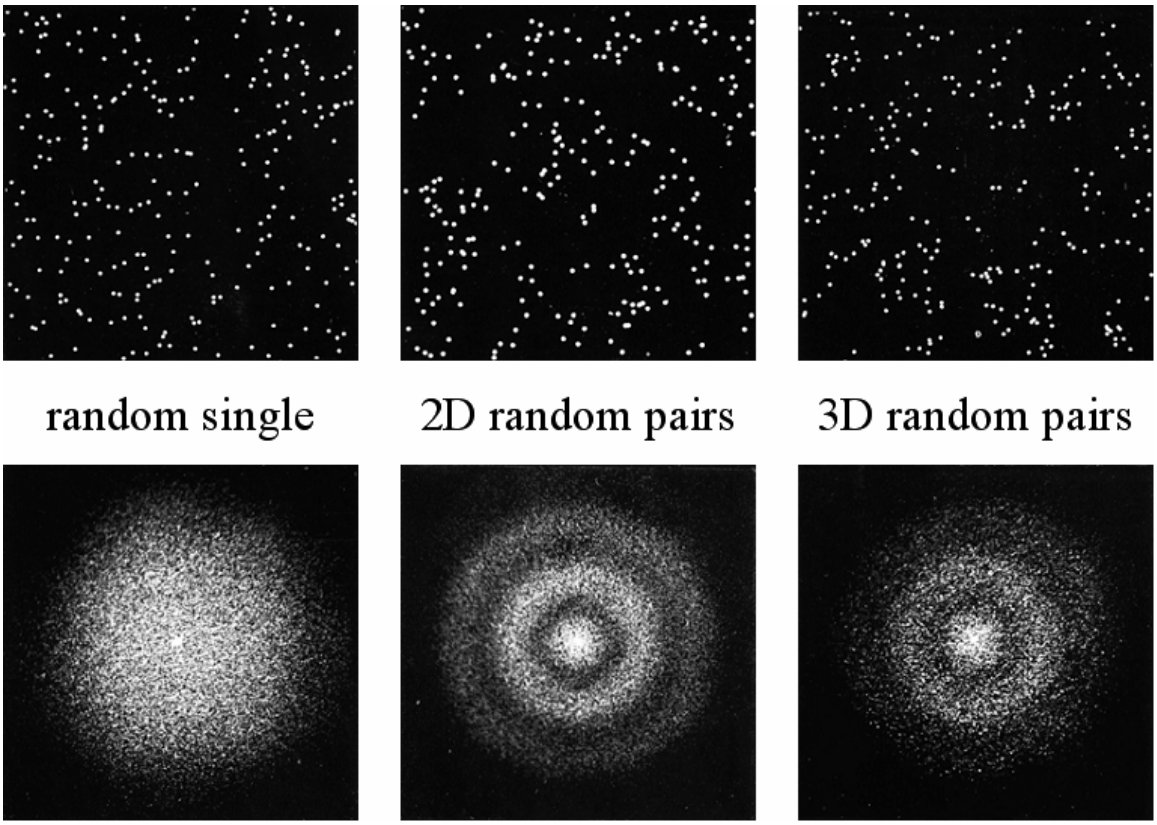

Figure 32: Detection of ordering with FFT, upper row is test images, lower row is corresponding Fourier transforms of test images.

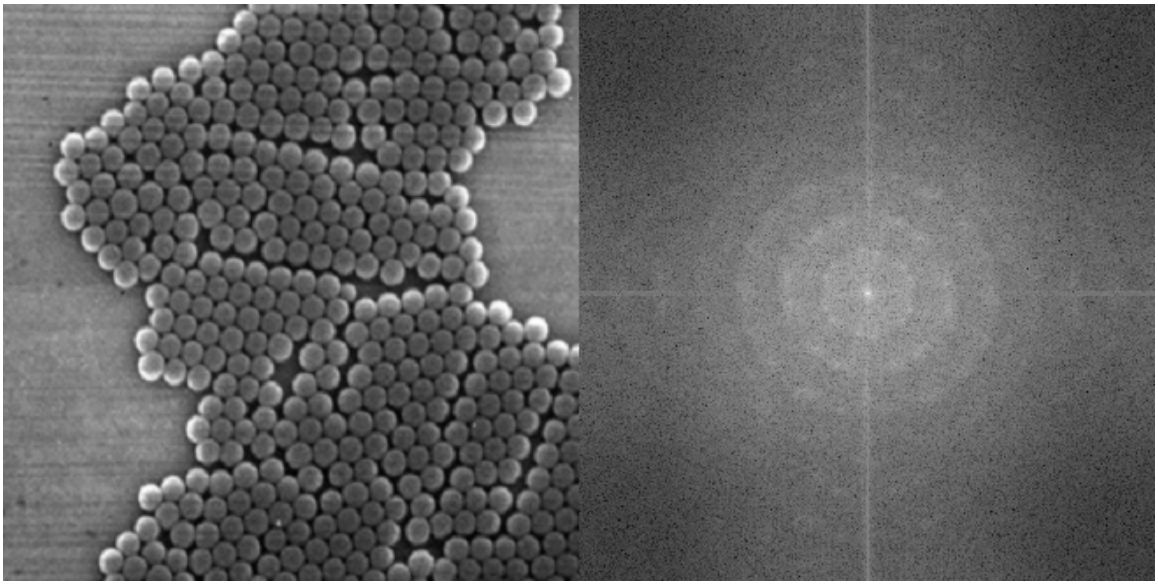

Figure 33: Example of high order detection using FFT.

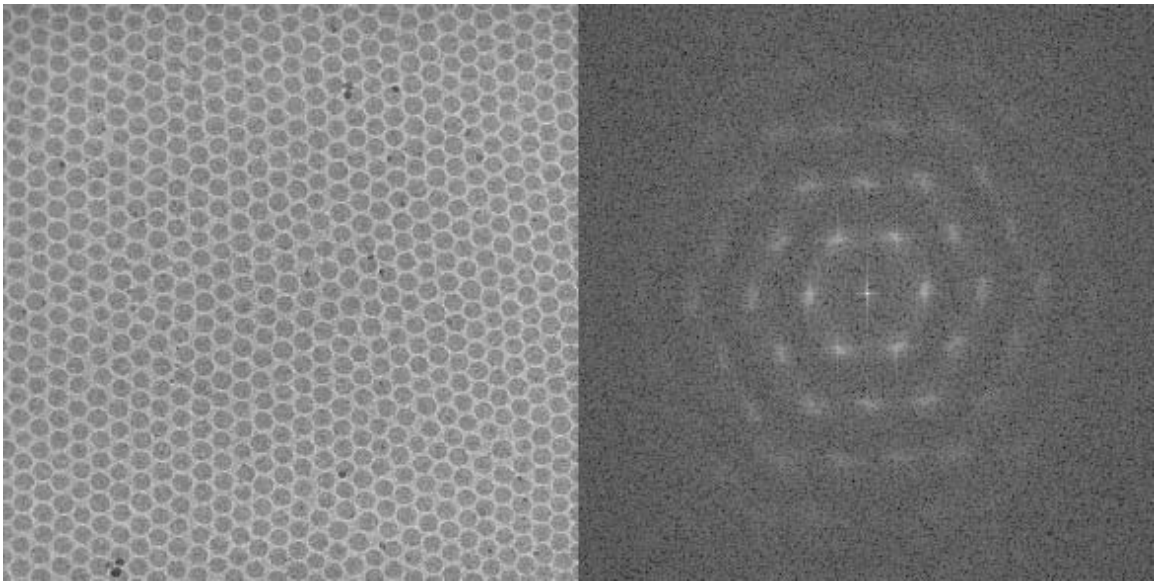

Figure 34: Example of high order detection in honey cone structure.

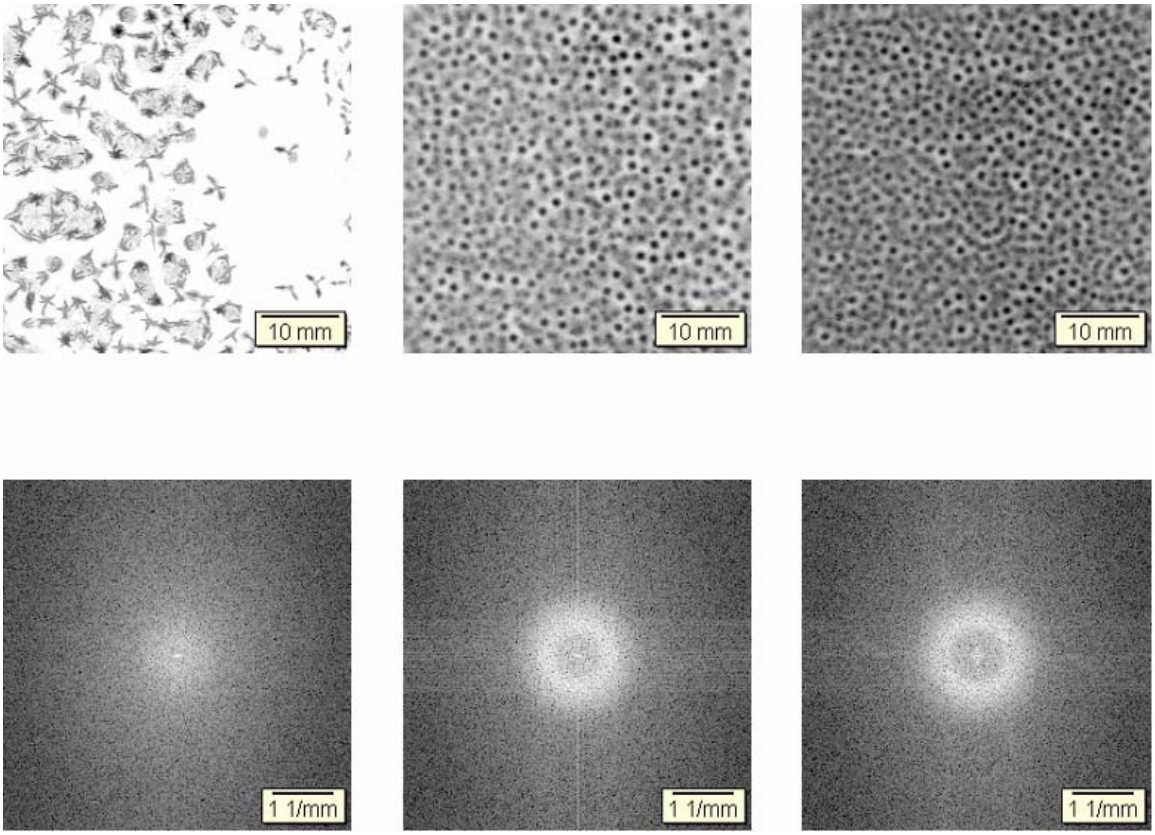

Figure 35: Order detection in experimental DBD images using FFT.

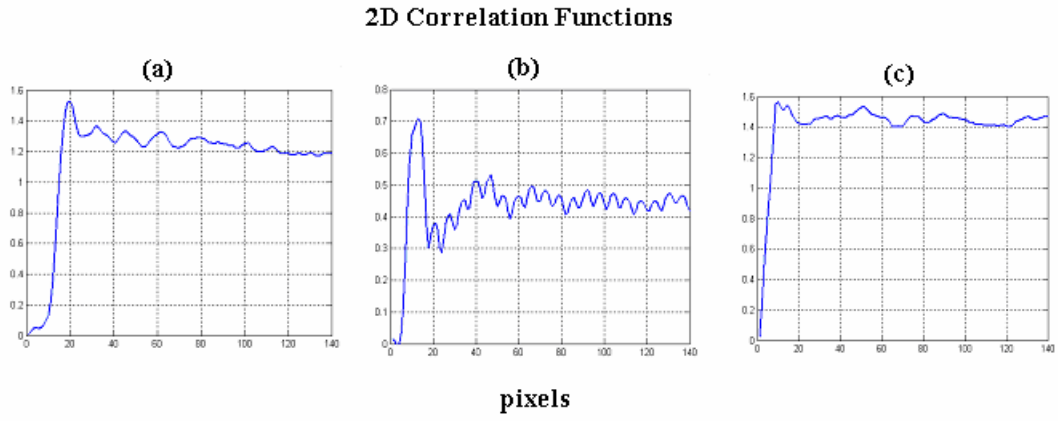

Figure 36: 2D correlation functions: (a) of experimental image from Figure 4; (b) of simulation data from Figure 20; (c) of data form random-point distribution (shown for comparison).

3.7 Gas Phase Plasma Chemistry in DBD: Effect of Vibrational Excitation.

Chemistry model of Dielectric Barrier Discharge (DBD) in humid air ($N_2/O_2/H_2O$) has been developed and applied for simulation of the plasma chemistry in experimental discharge setup. As we can see from previous chapters dielectric barrier discharge is a complex phenomena from physics point of view and it was important to understand and build the simplify model of such discharge which can be used for chemistry modeling. To achieve this we made a computational modeling of translational temperature depending on system geometry, energy input and gas nature, and further, analytical modeling of vibrational temperature depending on an electric power, gas flow rate and the geometry of the experimental system. Results of chemistry simulation show that NO_x concentration mainly depends on energy input and air humidity.

Lot of work was done in plasma remediation of NO_x from the gas stream in DBD by using dominant reactions of the removal of NO_x. In the present work we have another situation. In our case we use DBD for web treatment. Web treated by microdischarges to activate the surface and further to cover it by an emulsion. During the treatment microdischarges can produce undesirable concentration of NO_x. Molecules of NO_x can be attached to the surface of the web causing quality related problems with web coating. The goal of chemistry calculation was to analyze mechanisms responsible for NO_x production in dielectric barrier discharge.

In this work we took into account not only an electron temperature but also level of vibrational excitation which is of paramount importance for discharges in molecular gases. A new method of calculation of the vibrational temperature was implemented

which is included into the reactions rate constants. Multi-Streamer interaction has been shown to have strong effect on gas phase chemistry.

Due to specific geometry of experimental setup, comprehensive modeling of heat and gas fluxes was made using FLUENT software. Taking into account experimental data about discharge power, air mass flow and setup geometry. It gave us translational temperature distribution (see range in Table 4) and flow rate in the discharge zone which was used for prediction of vibrational temperature. Two cases were considered: when web is moving and when it's stationary. Web motion have a very little effect if any on memory effect, thus, was not considered in simulations of Multi-Streamer interaction. In contrast, web motion has significant effect on translational as well as vibrational temperatures. In case of stationary web flow rate trough discharge gap depend on inlet velocity linearly, in case of moving web flow rate is almost constant and does not depend on inlet velocity (for inlet velocity in same range). As we would expect in case of moving web, flow rate through discharge gap defined by the web velocity.

Table 4: Translational temperature range in the gap in critical conditions

Web	Discharge Power, Watt	Inlet velocity, m/s	Temperature Range, K
Stationary	150	0.0117	300 - 511
Moving	150	0.0117	300 - 397

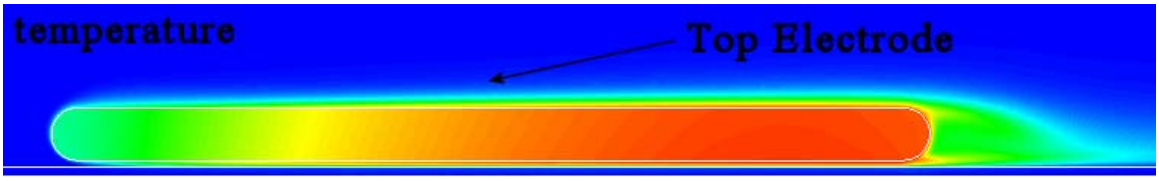

Figure 37: Temperature distribution in DBD, case of moving web conditions from Table 4. Gas flow is from left (inlet) to right (outlet).

For chemistry calculation we represent the streamer with simple analytical description: "tadpole" representation. We divide streamer into two parts from the electron concentration point of view. First part is a 'tail' – weekly ionized plasma channel; the second part is a 'head' – a cloud of positively charged ions. Of course, there is no sharp border between them. The electron concentration in 'head' remains almost constant $n_{\text{head}} = 10^{13}$ (cm^{-3}) during the whole path, while the electron concentration in the 'tail' is varied with the following equation [40]:

$$N_{tail} = N_{head} \cdot \exp(\frac{-t \cdot \mu \cdot E_0}{d})$$
$$t_0 = (\alpha \cdot \mu \cdot E_0)^{-1}$$

where t_0 - life-time of the 'head', $\mu \times E_0 = 10^7$ cm/s – drift velocity of the electrons, d - distance between electrodes, α - the first Townsend coefficient [1].

For rough estimation of vibrational temperature we used synergetic approach. The higher specific power $W/Q \rightarrow$ the higher vibrational temperature $T_V \rightarrow$ the longer EEDF (electron energy distribution function) $f(\varepsilon) \rightarrow$ the higher dissociation rate coefficient k_d.

Influence of vibrational excitation of molecules by electron impact on the electron energy distribution function is very strong in molecular gases [41]:

$$P_{eV} >> \frac{2m}{M}\frac{\varepsilon}{\hbar\omega},$$

where $P_{eV}(\varepsilon)$ is the probability of vibrational excitation, M and m are the neutral particle and electron masses, ε is an electron energy, $\hbar\omega$ is vibrational excitation energy of molecules. If we suppose, that $P_{eV}(\varepsilon) = const$ in some energy interval $\varepsilon_1 < \varepsilon < \varepsilon_2$, then the electron energy distribution function in the energy interval $\varepsilon_1 < \varepsilon < \varepsilon_2$ can be presented as:

$$f(\varepsilon) \propto \exp\left[-\frac{6P_{eV}\hbar\omega}{(eE\lambda)^2}\varepsilon\right],$$

where λ is a mean free electron path along the electric field. The fall of the electron energy distribution function in this energy interval can be described by the following small factor:

$$\alpha_v = \frac{f(\varepsilon_2)}{f(\varepsilon_1)} \approx \exp(-\frac{2M}{m}P_{eV}\hbar\omega\frac{\varepsilon_2-\varepsilon_1}{<\varepsilon>^2})$$

where $<\varepsilon>$ is the average electron energy of the Druyvesteyn distribution. The ionization and electronic excitation rate coefficients are proportional to the parameter α_v. The parameter α_v can be used for this reason to analyze the influence of vibrational temperature T_v on the ionization and electronic excitation rate coefficients [41]:

$$\alpha_v \approx \exp[-\frac{2M}{m}P_{eV}^0\hbar\omega\frac{\varepsilon_2-\varepsilon_1}{<\varepsilon>^2}(1-\exp(-\frac{\hbar\omega}{T_v}))]$$

Here P_{eV}^0 is the vibrational excitation probability of non-excited molecules (T_v = 0). Framework for vibrational excitation calculation presented in Figure 38. First specific power that goes to vibrational excitation calculated tacking into account cross section of vibrational excitation and relaxation of vibrational excitation on the walls as well as in the volume. Quant of vibrational excitation is higher than the average vibrational energy that is why we use Plank equation to find the average vibrational temperature. Vibrational temperature calculated from previous step used to estimate the changes in electron energy distribution function (EEDF) caused by vibrational excitation, see reference [41] for detailed discussion. Dependence of EEDF on level of vibrational excitation leads to dependence of reaction rates not only on electron temperature but also on vibrational

temperature. Effect of vibrational excitation on ionization coefficient is shown in Figure 39.

$$E_v \longrightarrow E_v = \frac{\hbar\omega}{\exp(\frac{\hbar\omega}{kT_v}) - 1}$$

$$\hbar\omega(N_2) = 0.2\ eV$$

$$\downarrow kT_v$$

$$\varphi(T_v) = \exp(b \cdot \exp(-\frac{\hbar\omega}{kT_v}))$$

$$\downarrow \varphi(T_v)$$

$$K_e(T_e, T_v) = \varphi(T_v) \cdot K(T_e)$$

Figure 38: Framework for vibrational excitation calculations.

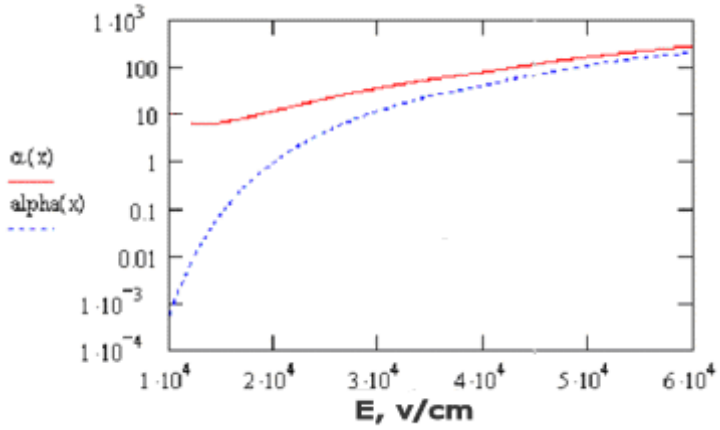

Figure 39: Effect of vibrational excitation on ionization coefficient. Blue curve is ionization coefficient; red curve is ionization coefficient with effect of vibrational excitation in red. Note that vibrational excitation has stronger effect in weaker electric field.

The chemical kinetics computational code uses CHEMKIN II gas-phase libraries and includes routines that implement effect of vibrational excitation described above. For detailed chemistry reaction mechanism see Appendix A. Humid air plasma gas-phase reaction mechanism that included 327 reactions and 57 species with point on NO_x production was created.

Dependences of NO_x concentration on time, power input and humidity are presented in Figure 40 - Figure 43. These results demonstrate that NO_x production increases with increasing of power input and humidity. As you see, in all these cases concentration always goes on some level of saturation. We also considered NO_x production in case of moving and stationary web to compare these two results and once more be sure that the level of saturation exists (Figure 43).

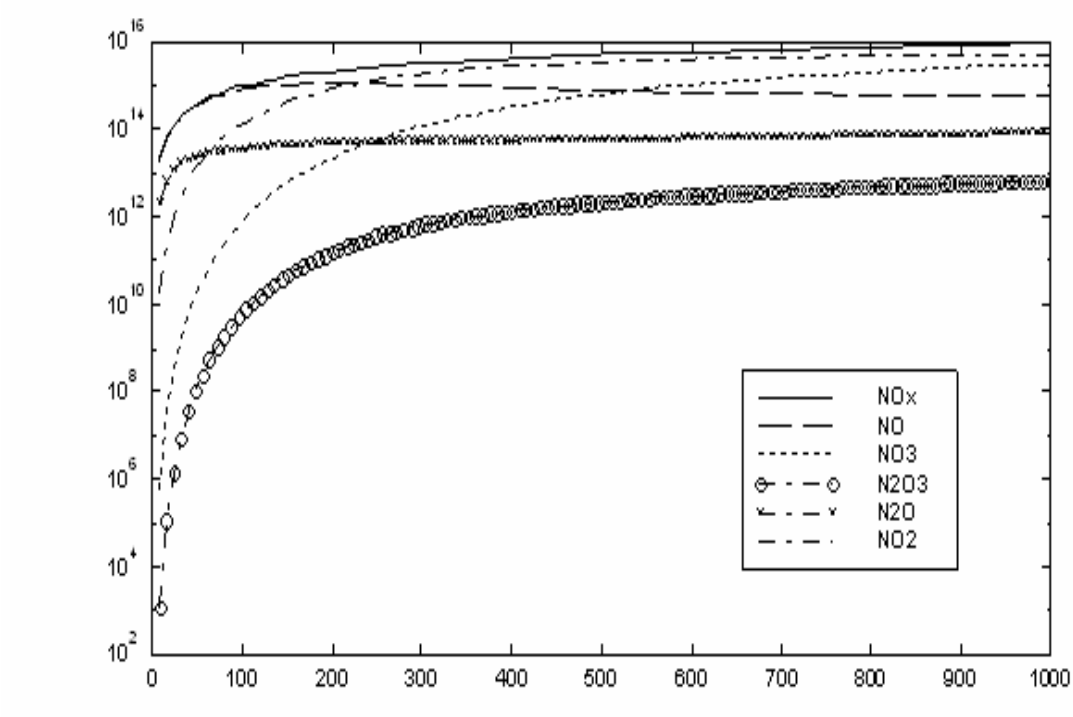

Figure 40: NOx production with no vibrational excitation, relative humidity is 40%.

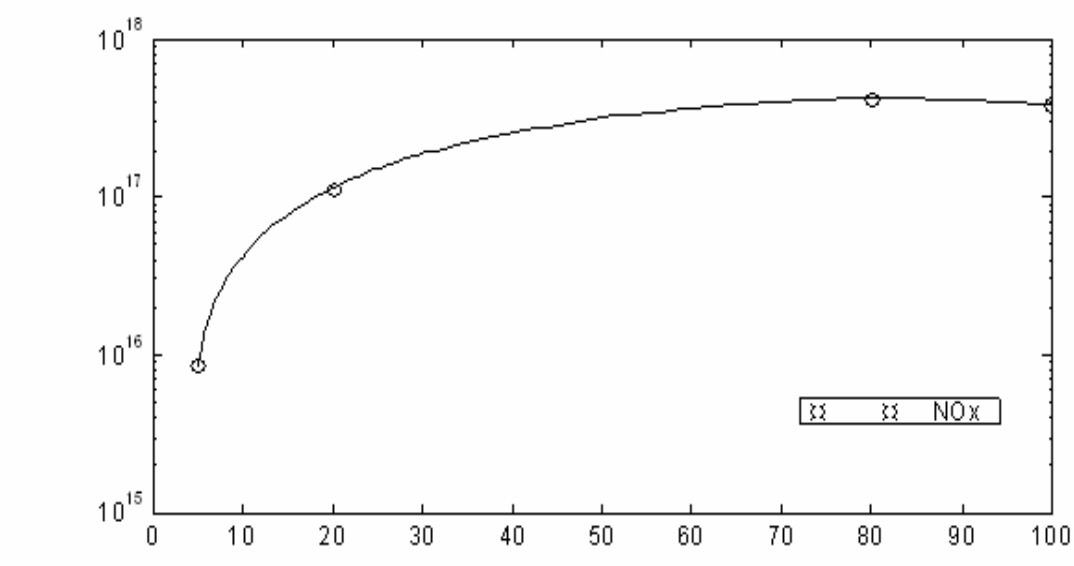

Figure 41: Maximum concentration of NOx production depending on vibrational excitation (power input). Relative humidity is 40%.

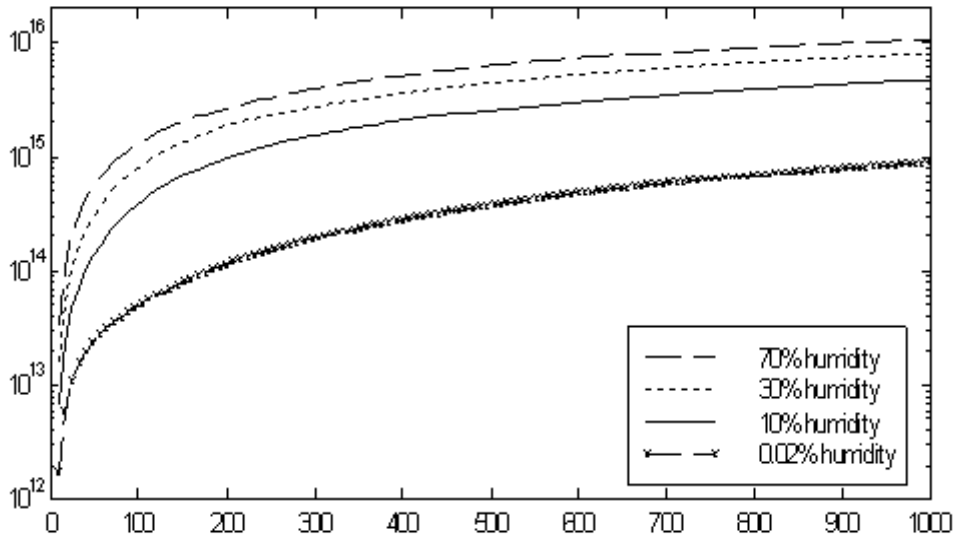

Figure 42: NO_x production depending on humidity

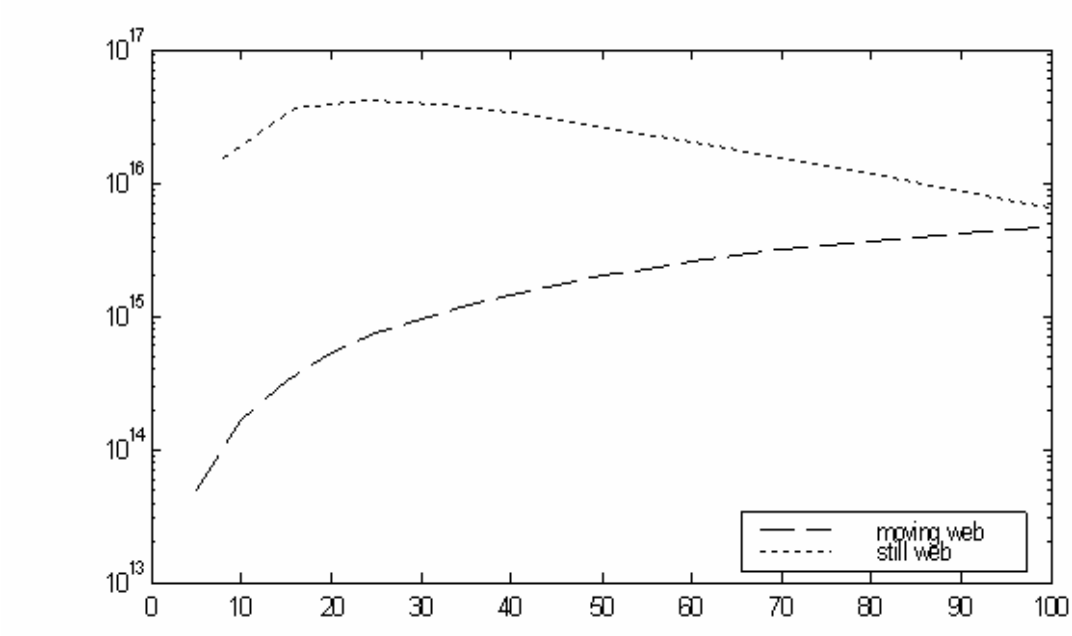

Figure 43: NO_x production in two regimes: moving web and still web, power equals 20 Watt, relative humidity 40%.

CHAPTER 4: RESULTS AND DISCUSSIONS

4.1 Multi-Streamer Patterns; Impact on Chemistry in DBD

Combining the results of chemistry calculations with Multi-Streamer interaction modeling one can describe the affect of interaction on chemistry. In order to do this we define the specific power input to each CA cell based on the results of simulations. Specific discharge power supplied into the cell was taken into account in chemistry calculations in each cell and then the results were averaged over the entire discharge gap. If there is a linear dependence between specific power and rate of production of species this procedure would not change the results based on the average specific power. This idea described in the following equation (where both of the averaging procedures are shown):

$$\hat{R}(p) = \frac{1}{N}\sum_{i=1}^{N} R(p_i)$$

$$\widetilde{R}(p) = R(\frac{1}{N}\sum_{i=1}^{N} p_i)$$

As you can see from Figure 41, NO_x production depends on specific power in non-linear fashion, similar behavior can be observed for many radicals produced in the discharge [37, 8]. Non-linear dependence on specific power leads to dependence of discharge chemistry in DBD on pattern formation and, thus, on Multi-Streamer interaction. Typical simulation result of this effect is presented in

Figure 44 that shows NOx production depending on the average specific power with power input distributed among discharge cells according to Figure 20. At high specific

power inputs chemistry in the discharge activated by energetic electrons mostly works in saturation regime, thus, uneven distribution of microdischarges leads to decreasing efficiency compared to homogenous distribution. Homogenous distribution of specific power corresponds to the case with no interaction between streamers and can be simulated by random streamer strikes, see Figure 25 and Figure 30. At lower specific power, as we can see from the heterogeneous distribution of microdischarges, we have the opposite effect on chemistry. But at the lower specific power Multi-Streamer interaction has little effect on microdischarge pattern; there should be enough microdischarges for the interaction works.

Multi-Streamer interaction leads to the reduction of radical production. The higher the interaction between the streamers the slower production rate of radicals will be. Degradation of the performance can be partially avoided by controlling pattern formation in dielectric barrier discharge. For the ideas in controlling the pattern formation see in the next chapter.

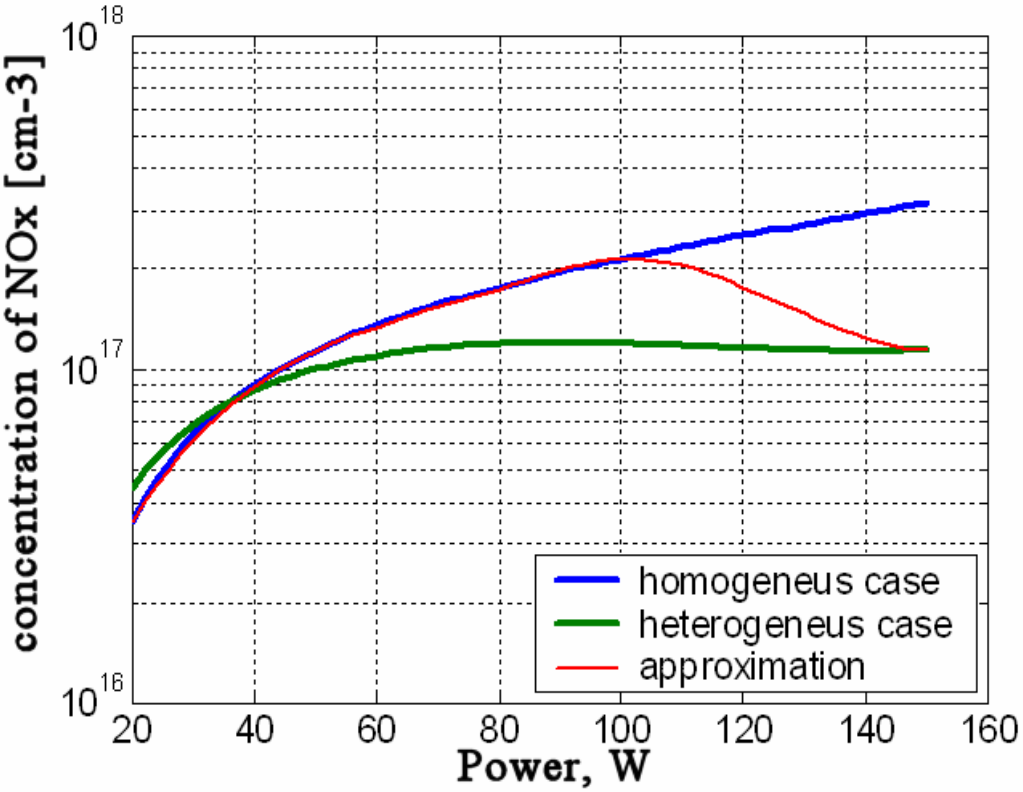

Figure 44: Impact of Multi-Streamer interaction on chemistry.

4.2 Effect of Applied Voltage on Multi-Streamer Patterns

Using Multi-Streamers interaction model we simulated pattern formation at different magnitudes of applied voltage. The sine voltage was used for this simulation. Voltage amplitude is represented as the percentage from Meeks voltage: minimum voltage required for streamer breakdown. As we increase voltage amplitude more streamers are formed each period interaction become stronger and distance between streamers decreases resulting in stronger pattern Figure 45. We find out in previous

chapter that stronger patterning leads to decreasing chemical performance. Thus, increasing an amplitude of applied voltage we effectively increase production of chemical species but the rate of production per specific energy input is expected to be smaller than at the lower voltages. This statement is in a good qualitative agreement with experimental data [4, 11].

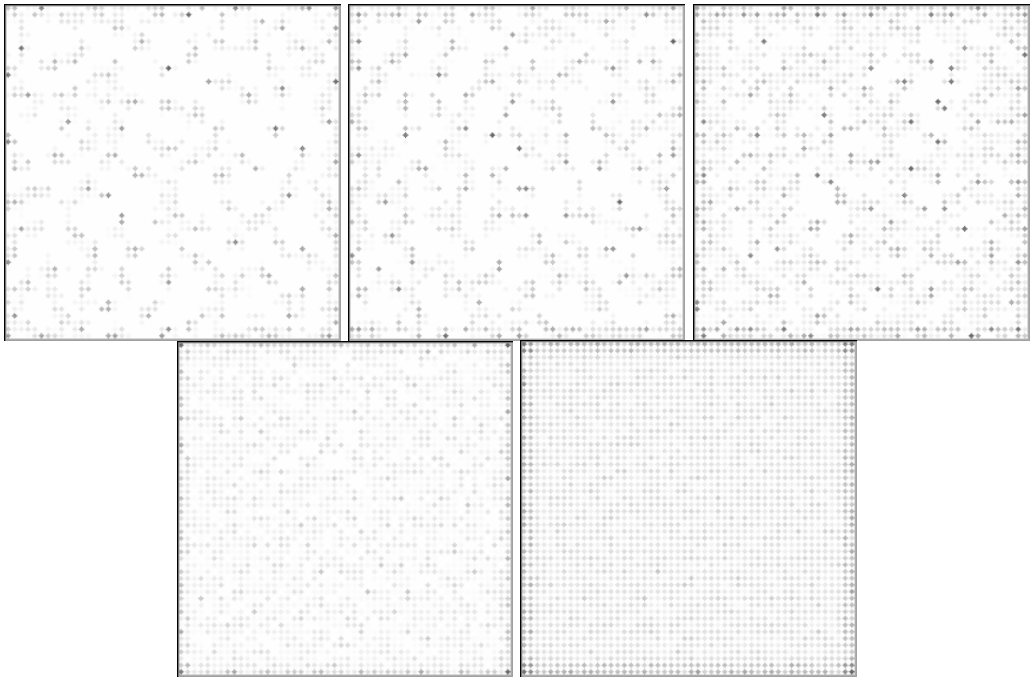

Figure 45: Effect of applied voltage on Multi-Streamer patterns. Shown voltages: 100%, 120%, 130%, 150%, and 200% from breakdown voltage (Meeks voltage).

LIST OF REFERENCES

1. Linsley Hood J. Int. Conf. On Gas Discharges and their Applications. Edinburgh 1980:86-90.

2. Uehara T. in: Adhesion Promotion Techniques, Mittal KL, Pizzi A (Eds.), Marcel Dekker, New York 1999:139-174.

3. Morrow R, Lowke JJ. Streamer propagation in air. J. Phys. D: Appl. Phys. 1997; 30:614–627.

4. Penetrante BM, Schultheis SE. Non-Thermal Plasma Techniques for Pollution Control, NATO ASI Series Parts A and B (Berlin: Springer) 1993.

5. Masuda S. Non-Thermal Plasma Techniques for Pollution Control, NATO ASI Series. Penetrante BM, Schultheis SE, Part B (Berlin: Springer) p 131.

6. Buss K. Arch. Elektrotech. 1932;26:261-265.

7. Babaeva NY, Naidis GV. Electrical Discharges for Environmental Purposes. Van Veldhuizen EM, Ed., Nova Science Publishers, Huntington, New York, NY, USA 2000:21-48.

8. Kulikovsky AA. Phys. Rev. E 57 1998:7066-707.

9. Eliasson B, Hirth M, Kogelschatz U, J. Phys. D: Applied Phys. 20 1987:1421-1437.

10. Rosenthal D. Electrical Characterization of Corona Discharge for Surface Treatment. IEEE Transactions on Industrial Applications 1976;1a-11(3):328-335.

11. Penetrante BM, Bardsley JN, Hsiao MC. Jpn. J. Appl. Phys. 1997; 36:5007-5017.

12. Fridman A, Kennedy L. Plasma Physics and Engineering. Taylor & Francis 2001.

13. For a recent review of the diverse phenomenon in barrier discharges see Kogelschatz U. in IEEE Trans of Plasma Science 2002;30(4):1400-1408.

14. Falkenstein Z, Coogan JJ. J. Phys. D: Appl. Phys. 1997;30:817-825.

15. Kodak TR#298611A, by Botticelli V, Soper R, Robinson K. Digital Measurement of Corona Discharge.

16. Lofthus A, Krupenie PH. J. Phys. Chem. Ref. Data 1977;6(1):113-307 (table 82).

17. Eliasson B, Kogelschatz U. IEEE Transactions on Plasma Science 1991;19(2): 309-323.

18. The authors thank and acknowledge Mr. David Steklenski of Kodak Health Imaging for providing the imaging plates used in this study.

19. Lichtenberg GC. Novi. Comment. Gott. 1777;8:168.

20. For an interesting paper on Lichtenberg figures see Merrill FH, Von Hipple A in J. Appl. Phys. 1939;10:873-887.

21. Anemiya Y. Journal of Synchrotron Radiation 1995;2(1):13-21.

22. Takahashi K, Tazaki S. Neriishi K, Etoh M. Fujifilm Research and Development 1998;43:41-46.

23. Ben-Kish A, Fisher A, Cheifetz E, Schwob JL. Review of Scientific Instruments 2000;71(7):2651-2654.

24. Katto M, Kurosawa K, Sasaki W, Takigawa Y, Okuda M. Japanese Journal of Applied Physics, part 1: Regular papers, Short notices & Review Papers 1991;30(11a):2806-2807.

25. Johnston RF, Pickett SC, Barker DL. Electrophoresis 1990;11(5):355-360.

26. Matsuda K., Kijima T, Atsumi H, Tsuji Y, Hatado M. RadTech Asia '91, Conf. Proc. Publisher: RadTech Int. North A,. Northbrook, Ill. 1991;4:540.

27. Keller DS, Pawlak JJ. Journal of Pulp and Paper Science 2001;27(4):117-123.

28. Eliasson B, Kogelschatz U. IEEE Trans Plasma Sci. 1991;19(2):309.

29. Peyrous R, Pignolet P, Held B. J. Phys. D: Appl. Phys. 1989;22(11):1658-1667.

30. Gunter Steinle and etc. J. Phys. D: Appl. Phys. 1999;32:1350-1356.

31. Niemeyer L, Pietronero L, Wiedmann HJ. Phys. Rev. Letters 1984;52:12.

32. Aints A, Ahaljaste KK, Plank T. J. Phys. D: Appl Phys 1997;30:210-220.

33. Zuzic M et al. Phys. Rev. Lett., November 6, 2000;85(19):4064-4067.

34. Thomas H et al. Phys. Rev. Lett., August 1, 1994;73(5).

35. Iskenderova K, Chirokov A, Gutsol A, Fridman A. Two-dimensional modeling of spontaneous pattern formation in dielectric-barrier discharge system. 16th International Symposium on Plasma Chemistry 2003.

36. Chirokov A, Gutsol A, Fridman A, Sieber KD, Grace JM, Robinson KS. Two-dimensional microdischarge distribution in Dielectric-Barrier Discharges. Plasma Chemistry Plasma Processing, (to be published) 2003.

37. Chirokov A, Iskenderova K, Gutsol A, Fridman A, Kennedy L, Sieber K, Grace J, Robinson K. Simulation of nox formation in dielectric barrier discharge. Proc. 15th Intn. Symp. On Plasma Chemistry 2001;2:443-448.

38. Harburn, Taylor, Welbeny, Atlas of Optical Transforms.

39. FFTW library: http://www.fftw.org/

40. Raizer YP. Gas discharge physics. Springer 1997.

41. Fridman A, Kennedy L. Plasma Physics and Engineering. Taylor & Francis 2001.

APPENDIX A: HUMID AIR GAS PHASE REACTION MECHANISM

Reaction rate calculated from Arrhenius equation is given below. Reaction mechanism used for chemistry calculation [37] is presented in Table 5.

$$k = A \cdot T^{b} \cdot \exp(\frac{-E}{R \cdot T})$$

Table 5: Reaction Mechanism, *A* units mol-cm-s-K, *E* units cal/mol

#	Reactions Considered	A	b	E
1	O2+E=>O2++2E	1.76E+14	0.0	0.0
2	O2+E=>O2a1D+E	2.88E+15	0.0	0.0
3	O2+E=>O2B1S+E	2.88E+15	0.0	0.0
4	O2+E=>O2-	6.00E-08	0.0	0.0
5	O+E=>O++2E	5.40E+15	0.0	0.0
6	O+E=>O1D+E	2.52E+15	0.0	0.0
7	O+E=>O1S+E	2.52E+15	0.0	0.0
8	N2a+E=>N2++2E	1.32E+17	0.0	0.0
9	N2A+E=>N2++2E	1.32E+17	0.0	0.0
10	NO2++E=>NO+O	1.20E+15	0.0	0.0
11	NO2++E=>NO+O1D	1.20E+15	0.0	0.0
12	E+NO2=>NO2-	2.40E+16	0.0	0.0
13	N2+E=>N2A+E	5.10E+13	0.0	0.0
14	N2+E=>N2a+E	5.10E+13	0.0	0.0
15	N2+E=>N2++2E	3.99E+11	0.0	0.0
16	O2+E=>O+O+E	8.60E+14	0.0	0.0
17	O2+E=>O-+O	3.62E+13	0.0	0.0
18	O2a1D+E=>O+O+E	2.88E+17	0.0	0.0
19	O2a1D+E=>O2++2E	2.88E+17	0.0	0.0
20	O2B1S+E=>O+O+E	2.88E+17	0.0	0.0
21	O2B1S+E=>O2++2E	2.88E+17	0.0	0.0
22	N2O+E=>N2+O-	2.88E+17	0.0	0.0
23	NO++E=>N+O1D	2.40E+13	0.0	0.0
24	O3+E=>O3++2E	3.00E+14	0.0	0.0
25	H2O+E=>H+OH+E	3.18E+13	0.0	0.0
26	H2O+E=>O1D+H2+E	3.54E+13	0.0	0.0
27	H2O+E=>H2O++2E	3.90E+13	0.0	0.0
28	H2O+E=>OH-+H	1.50E+14	0.0	0.0
29	H2O+E=>H-+OH	1.50E+14	0.0	0.0
30	H2O+E=>H2+O-	1.50E+14	0.0	0.0

Table 5 (continued): Reaction Mechanism, *A* units mol-cm-s-K, *E* units cal/mol

31	E+N2+=>N+N	3.24E+16	-0.4	0.0
32	E+N2++O2=>N2+O2	6.00E-03	0.0	0.0
33	E+O2+=>O+O	1.62E+16	-0.6	0.0
34	E+O2+=>O+O1D	1.17E+17	0.0	0.0
35	E+O2++O2=>O2+O2	4.80E-05	0.0	0.0
36	E+NO+=>N+O	3.96E+16	-0.5	0.0
37	E+NO++O2=>NO+O2	1.86E+01	-1.5	0.0
38	E+N4+=>N2+N+N	1.20E+18	0.0	0.0
39	E+O4+=>O2+O+O	1.20E+18	0.0	0.0
40	E+O4+=>O2+O2	6.60E+16	0.0	0.0
41	E+O++E=>O+E	5.25E-03	-4.5	0.0
42	E+H2O+=>H+OH	6.60E+17	-0.5	0.0
43	E+H2O+=>O+H2	2.28E+17	-0.5	0.0
44	E+H2O+=>O+H+H	2.88E+17	-0.5	0.0
45	E+H3O+=>H2O+H	1.32E+18	-0.1	0.0
46	E+O2+O2=>O2-+O2	1.32E-06	0.0	0.0
47	E+O2+N2=>O2-+N2	6.00E-08	0.0	0.0
48	E+O+O2=>O-+O2	6.00E-08	0.0	0.0
49	E+O+N2=>O-+N2	6.00E-08	0.0	0.0
50	E+HO2=>H+O2-	3.00E+15	0.0	0.0
51	E+NO2=>O-+NO	2.04E+14	-2.4	3.0
52	E+O3=>O-+O2	6.00E+12	0.0	0.0
53	E+O=>O-	7.80E+08	0.0	0.0
54	E+O3+O2=>O3-+O2	2.76E-04	0.0	0.0
55	E+NO=>O-+N	2.04E+18	-8.2	15.2
56	E+NO+N2=>NO-+N2	2.40E-05	0.0	0.0
57	E+HNO2=>NO2-+H	3.00E+16	0.0	0.0
58	E+HNO3=>NO2-+OH	3.00E+16	0.0	0.0
59	E+N2O+N2=>N2O-+N2	1.80E-09	0.0	0.0
60	E+O3=>O2+O+E	1.34E+16	0.0	0.0
61	O+O+N2=>O2+N2	3.90E-11	0.0	-1039.0
62	O+O+N=>O2+N	3.90E-11	0.0	-1039.0
63	O+O2+O2=>O3+O2	1.45E-10	-1.0	-238.9
64	O+O2+N2=>O3+N2	1.45E-10	-1.0	-238.9
65	O+O2+O3=>O3+O3	8.58E-10	-2.0	0.0
66	O+O2+O=>O3+O	1.29E-10	0.0	-345.0
67	O+O3=>2O2	9.17E+12	0.0	2185.0
68	O+NO+N2=>NO2+N2	6.38E-08	-1.7	46.3
69	O+NO+O2=>NO2+O2	6.38E-08	-1.7	46.3
70	O+NO=>NO2	1.33E+13	0.5	-92.6
71	O+NO=>O2+N	2.53E+13	0.0	23200.0
72	O+NO2=>O2+NO	5.45E+12	0.2	0.0
73	O+NO2=>NO3	1.32E+13	0.0	0.0

Table 5 (continued): Reaction Mechanism, *A* units mol-cm-s-K, *E* units cal/mol

74	O+NO2+N2=>NO3+N2	6.39E-08	-2.2	46.6
75	O+NO2+O2=>NO3+O2	6.39E-08	-2.2	46.6
76	O+NO3=>O2+NO2	6.00E+12	0.0	0.0
77	N+N+N2=>N2+N2	4.96E-10	0.0	-500.0
78	N+N+N=>N2+N	1.40E-09	0.0	-500.0
79	N+NO=>N2+O	2.11E+13	0.0	49.8
80	N+O2=>NO+O	6.01E+12	0.0	3473.0
81	N+NO2=>N2O+O	1.80E+12	0.0	0.0
82	N+O3=>NO+O2	6.00E+07	0.0	0.0
83	NO+O3=>O2+NO2	2.58E+12	0.0	1560.0
84	NO2+O3=>NO3+O2	1.14E+11	0.0	2542.0
85	NO3+O3=>2O2+NO2	7.20E+10	0.0	2450.0
86	NO+NO2+N2=>N2O3+N2	5.47E-09	0.0	0.0
87	NO+NO2=>N2O3	2.04E+12	0.0	0.0
88	NO+NO3=>2NO2	6.66E+12	0.0	-220.9
89	H+O2=>O+OH	7.01E+13	0.3	7860.0
90	H+O2+1H2=>1HO2+1H2	3.47E-08	-0.8	0.0
91	H+O2+1N2=>1HO2+1N2	3.56E-08	-1.0	0.0
92	H+O2+1O2=>1HO2+1O2	3.56E-08	-1.0	0.0
93	H+OH+1N2=>1H2O+1N2	3.56E-08	-1.0	0.0
94	H+OH+1O2=>1H2O+1O2	4.13E-07	-2.0	0.0
95	H+OH+H2O=>H2O+H2O	2.62E-06	-2.0	0.0
96	H+NO2=>NO+OH	1.32E+14	0.0	182.0
97	H+1O3=>1O2+1OH	4.67E+13	0.3	327.8
98	H+1O3=>1HO2+1O	4.50E+11	0.0	0.0
99	H+1HO2=>1H2+1O2	1.54E+13	0.6	346.0
100	H+1HO2=>1OH+1OH	1.41E+14	0.0	373.7
101	H+1HO2=>1H2O+1O	5.51E+13	0.0	971.9
102	H+1O2=>1HO2	4.50E+13	0.0	0.0
103	H+1OH=>1H2O	1.62E+10	0.0	0.0
104	H+HNO=>H2+NO	2.56E+12	0.0	-998.1
105	H+1HNO=>1OH+1NH	1.45E+15	-0.5	9010.0
106	H+1HNO=>1O+1NH2	6.30E+14	-0.3	14730.0
107	H+1NO=>1NH+1O	5.57E+14	-0.1	35220.0
108	H+1NO=>1OH+1N	1.27E+14	0.0	24330.0
109	H+1NO+1N2=>1HNO+1N2	4.40E-08	-1.3	184.3
110	H+1NO+1O2=>1HNO+1O2	4.40E-08	-1.3	184.3
111	H+1NO3=>1NO2+1OH	6.60E+13	0.0	0.0
112	H+1H2O2=>1OH+1H2O	2.40E+13	0.0	2000.0
113	H+1H2O2=>1H2+1HO2	4.80E+13	0.0	4000.0
114	OH+1OH=>1H2O+1O	9.29E+10	1.4	-267.3
115	OH+1O=>1O2+1H	1.26E+13	-0.2	153.9
116	OH+1H=>1H2+1O	6.74E+09	3.4	1233.0

Table 5 (continued): Reaction Mechanism, *A* units mol-cm-s-K, *E* units cal/mol

117	OH+1H2=>1H2O+1H	1.39E+12	1.5	1761.0
118	OH+1O3=>1HO2+1O2	8.83E+11	0.0	932.7
119	OH+1HO2=>1H2O+1O2	2.63E+13	0.0	-110.9
120	OH+1OH+1N2=>1H2O2+1N2	3.63E-07	-3.0	0.0
121	OH+1OH+1O2=>1H2O2+1O2	3.63E-07	-3.0	0.0
122	OH+1OH+1H2O=>1H2O2+1H2O	9.26E-08	-2.0	-183.6
123	OH+1H2O2=>1H2O+1HO2	2.72E+12	0.0	288.9
124	OH+1HNO2=>1H2O+1NO2	1.08E+13	0.0	390.0
125	OH+1N2O=>1HO2+1N2	2.22E+11	0.0	2740.0
126	OH+1OH=>1H2O2	9.06E+12	-0.4	0.0
127	OH+1NO+1N2=>1HNO2+1N2	2.35E-08	0.0	-794.2
128	OH+1NO+1O2=>1HNO2+1O2	2.35E-08	0.0	-794.2
129	OH+1NO2=>1HO2+1NO	1.98E+13	0.0	3360.0
130	OH+1NO2+1N2=>1HNO3+1N2	5.03E-06	-3.9	409.3
131	OH+1NO2+1O2=>1HNO3+1O2	5.03E-06	-3.9	409.3
132	OH+1NO3=>1HO2+1NO2	1.38E+13	0.0	0.0
133	OH+1HNO=>1H2O+1NO	7.60E+12	1.0	334.2
134	OH+1HNO3=>1H2O+1NO3	2.40E+10	0.0	-317.6
135	HO2+1O3=>1OH+2O2	1.05E+09	0.0	-628.3
136	HO2+1HO2=>1H2O2+1O2	1.80E+12	0.0	0.0
137	HO2+1O=>1OH+1O2	1.74E+13	0.0	-200.0
138	2HO2+N2=>H2O2+O2+N2	1.14E-09	0.0	-980.0
139	HO2+1HO2+1O2=>H2O2+2O2	1.14E-09	0.0	-980.0
140	HO2+1NO=>1O2+1HNO	5.46E+05	0.0	-2819.0
141	HO2+1NO=>1OH+1NO2	2.10E+12	0.0	-240.0
142	HO2+1NO2=>1HNO2+1O2	7.20E+10	0.0	0.0
143	HO2+1NO=>1HNO3	8.40E+10	0.0	0.0
144	HO2+1N=>1OH+1NO	1.32E+13	0.0	0.0
145	HO2+1NO3=>1HNO3+1O2	5.53E+11	0.0	0.0
146	N+1OH=>1NO+1H	2.35E+13	0.0	-72.4
147	N+1OH=>1O+1NH	1.13E+13	0.1	10700.0
148	O+1H2=>1OH+1H	9.01E+10	2.8	2834.0
149	O+1H2O2=>1OH+1HO2	1.08E+11	2.9	1394.0
150	N2O3+1H2O=>2HNO2	3.78E+13	0.0	4468.0
151	HNO2+1O=>1OH+1NO2	6.00E+08	0.0	0.0
152	HNO3+1O=>1OH+1NO3	1.80E+07	0.0	0.0
153	HNO2+1NO3=>1HNO3+1NO2	1.20E+09	0.0	0.0
154	H2O2+1NO3=>1HO2+1HNO3	1.20E+09	0.0	0.0
155	N2A+H2O=>H2+N+NO	6.00E+13	0.0	0.0
156	N2a+H2O=>H2+N+NO	6.00E+13	0.0	0.0
157	O1D+H2O=>OH+OH	1.20E+14	0.0	0.0
158	O1D+H2=>OH+H	1.98E+14	0.0	0.0
159	O1D+H2O2=>H2O+O2	3.12E+14	0.0	0.0

Table 5 (continued): Reaction Mechanism, *A* units mol-cm-s-K, *E* units cal/mol

160	O1S+H2O=>O+H2O	1.80E+14	0.0	0.0
161	O1S+H2O=>OH+OH	3.00E+14	0.0	0.0
162	O1S+H2O=>H2+O2	3.00E+14	0.0	0.0
163	O2a1D+H2O=>O2+H2O	3.00E+06	0.0	0.0
164	O2B1S+H2O=>O2+H2O	2.40E+12	0.0	0.0
165	O++H2=>OH++H	6.00E+13	0.0	0.0
166	O++H2O=>H2O++O	1.56E+15	0.0	0.0
167	O2++2H2O=>H3O++OH+O2	1.20E-04	0.0	0.0
168	O4++2H2O=>H3O++OH+2O2	1.20E-04	0.0	0.0
169	N2++H2O=>H2O++N2	1.32E+15	0.0	0.0
170	H2O++O2=>H2O+O2+	1.98E+14	0.0	0.0
171	H2O++H2O=>H3O++OH	1.11E+15	0.0	0.0
172	OH++O2=>OH+O2+	2.28E+14	0.0	0.0
173	NO++2H2O=>H3O++HNO2	1.20E-04	0.0	0.0
174	O-+H2=>H2O+E	3.90E+14	0.0	0.0
175	O2-+1H2O=>1O2+1H2O+E	3.00E+15	0.0	5000.0
176	OH-+1O3=>1OH+1O3-	3.00E+14	0.0	0.0
177	OH-+1O3=>1O2-+1HO2	6.00E+12	0.0	0.0
178	H-+1H2O=>1OH-+1H2	6.00E+14	0.0	0.0
179	H3O++NO2-=>H2O+OH+NO	1.13E+18	0.0	0.0
180	H3O++O3-=>H2O+OH+O2	6.00E+17	0.0	0.0
181	H2O+O2+E=>O2-+H2O	8.40E-06	0.0	0.0
182	N2a+N2a=>N2+N2++E	6.00E+13	0.0	0.0
183	N2a+O2=>N2+2O	1.68E+13	0.0	0.0
184	N2a+N2=>N2+N2	1.20E+11	0.0	0.0
185	N2a+NO=>N2+N+O	2.16E+14	0.0	0.0
186	N2A+N2=>N2+N2	1.80E+06	0.0	0.0
187	N2A+O2=>N2+2O	7.74E+11	0.0	0.0
188	N2A+O2=>N2O+O	4.68E+10	0.0	0.0
189	N2A+NO=>N2+NO	4.20E+13	0.0	0.0
190	N2A+O=>NO+N	4.20E+12	0.0	0.0
191	N2A+O=>N2+O1S	1.26E+13	0.0	0.0
192	N2A+N=>N2+N	3.00E+13	0.0	0.0
193	N2A+N2O=>N2+N+NO	6.00E+12	0.0	0.0
194	O1D+N2=>O+N2	1.08E+13	0.0	-107.0
195	O1D+O2=>O+O2B1S	1.54E+13	0.0	-67.0
196	O1D+O2=>O+O2a1D	6.00E+11	0.0	0.0
197	O1D+NO=>O2+N	1.02E+14	0.0	0.0
198	O1D+NO2=>O2+NO	1.80E+14	0.0	0.0
199	O1D+N2O=>NO+NO	4.32E+13	0.0	0.0
200	O1D+N2O=>N+NO2	1.47E+11	0.0	0.0
201	O1D+N2O=>N2+O2	2.94E+13	0.0	0.0
202	O1D+O3=>2O+O2	7.20E+22	0.0	0.0

Table 5 (continued): Reaction Mechanism, *A* units mol-cm-s-K, *E* units cal/mol

203	O1D+O3=>2O2	1.44E+14	0.0	0.0
204	O1D+O3=>O+O3	1.44E+14	0.0	0.0
205	O1D+O3=>O2B1S+O2	2.16E+13	0.0	0.0
206	O1S+NO=>O2+N	3.00E+14	0	0.0
207	O1S+O2=>O2+O	1.80E+11	0.0	850
208	O1S+O3=>O2+O+O1D	1.74E+14	0.0	0.0
209	O1S+O3=>2O2	5.40E+13	0.0	0.0
210	O1S+O2a1D=>O2+O1D	3.60E+12	0.0	0.0
211	O1S+O2a1D=>3O	2.40E+12	0.0	0.0
212	O1S+O2a1D=>O+O2B1S	7.80E+13	0.0	0.0
213	O1S+O=>O+O1D	3.00E+12	0.0	301.0
214	O2a1D+N=>O+NO	1.20E+10	0.0	600.0
215	O2a1D+O=>O+O2	4.20E+10	0.0	0.0
216	O2a1D+NO=>NO+O2	1.50E+13	0.0	0.0
217	O2a1D+O3=>2O2+O	1.43E+12	0.0	2876.0
218	O2a1D+O2=>O2+O2	1.32E+23	0.8	0.0
219	O2a1D+N2=>O2+N2	8.40E+04	0.0	0.0
220	O2a1D+NO=>O+NO2	2.93E+06	0.0	0.0
221	O2B1S+N2=>O2a1D+N2	2.94E+09	0.0	253.0
222	O2B1S+O2=>O2a1D+O2	2.24E+08	2.4	241.0
223	O2B1S+O3=>2O2a1D+O	1.08E+13	0.0	0.0
224	O2B1S+O=>O2+O	4.80E+10	0.0	0.0
225	O2B1S+NO=>O2a1D+NO	2.40E+10	0.0	0.0
226	O++N2=>NO++N	1.80E+23	0.0	0.0
227	O2++NO=>O2+NO+	2.64E+14	0.0	0.0
228	O2++O2+N2=>O4++N2	1.44E+21	-3.2	0.0
229	O2++O2+N=>O4++N	1.44E-06	-3.2	0.0
230	O2++N=>NO++O	7.20E+13	0.0	0.0
231	O2++N2=>NO++NO	6.00E+06	0.0	0.0
232	O3++O2=>O2++O3	6.00E+12	0.0	0.0
233	O4++O2a1D=>O2++O2+O2	6.00E+13	0.0	0.0
234	O4++O2B1S=>O2++O2+O2	6.00E+13	0.0	0.0
235	O4++NO=>NO++O2+O2	6.00E+13	0.0	0.0
236	O4++O=>O3++1O2	1.80E+14	0.0	0.0
237	O4++O=>O2++1O3	1.80E+14	0.0	0.0
238	O4++O2=>O2++O2+O2	1.20E+11	0.0	0.0
239	N2++O=>N2+O+	6.00E+12	-0.2	0.0
240	N2++O=>NO++N	7.80E+13	-0.5	0.0
241	N2++O2=>N2+O2+	3.60E+13	-0.5	0.0
242	N2++NO=>N2+NO+	1.98E+14	0.0	0.0
243	N2++N2+N2=>N4++N2	3.00E-05	-1.0	0.0
244	N2++N2+N=>N4++N	3.00E-05	-1.0	0.0
245	N4++O2=>O2++N2+N2	1.50E+14	0.0	0.0

Table 5 (continued): Reaction Mechanism, *A* units mol-cm-s-K, *E* units cal/mol

246	N4++O=>O++N2+N2	1.50E+14	0.0	0.0
247	1O-+1N2=>1N2O+1E	6.00E+11	0.0	0.0
248	O-+1O2=>1O3+1E	3.00E+09	0.0	0.0
249	O-+1O=>1O2+1E	3.00E+14	0.0	0.0
250	O-+1N=>1NO+1E	1.56E+14	0.0	0.0
251	O-+1N2A=>1O+1N2+1E	1.32E+15	0.0	0.0
252	O-+1O2a1D=>1O3+1E	1.80E+14	0.0	0.0
253	O-+1O3=>2O2+1E	3.18E+14	0.0	0.0
254	O-+1NO=>1NO2+1E	1.56E+14	0.0	0.0
255	O-+1N2O=>1NO-+1NO	1.26E+14	0.0	0.0
256	O-+1NO2=>1O+1NO2-	7.20E+14	0.0	0.0
257	O-+1NO2=>1O2-+1NO	1.20E+13	0.0	0.0
258	O-+1O2+1O2=>1O3-+1O2	6.60E-07	0.0	0.0
259	O-+1O3=>1O3-+1O	3.30E+14	0.0	0.0
260	O-+1O3=>1O2-+1O2	6.00E+12	0.0	0.0
261	O2-+1O=>1O-+1O2	1.99E+14	0.0	0.0
262	O2-+1O=>1O3+1E	9.00E+13	0.0	0.0
263	O2-+1O2=>1O2+1O2+E	1.62E+06	0.5	559.0
264	O2-+1O2a1D=>1O2+O2+E	1.20E+14	0.0	0.0
265	O2-+1O2B1S=>1O2+O2+E	2.16E+14	0.0	0.0
266	O2-+1N2=>1O2+N2+E	6.60E+04	0.0	0.0
267	O2-+1NO2=>1NO2-+1O2	4.80E+14	0.0	0.0
268	O2-+1N=>1NO2+1E	3.00E+14	0.0	0.0
269	O2-+1O3=>1O2+1O3-	2.40E+14	0.0	0.0
270	O3-+1O=>1O2-+1O2	6.60E+12	0.0	0.0
271	O3-+1O=>2O2+1E	8.40E+13	0.0	0.0
272	O3-+1N2=>1NO2-+1NO	6.00E+03	0.0	0.0
273	O3-+1NO=>1NO3-+1O	6.00E+12	0.0	0.0
274	O3-+1NO2=>1O3+1NO2-	4.20E+14	0.0	0.0
275	O3-+1NO2=>1NO3-+1O2	1.20E+13	0.0	0.0
276	NO-+1O2=>1O2-+1NO	3.00E+14	0.0	0.0
277	NO-+1NO2=>1NO2-+1NO	4.44E+08	0.0	0.0
278	NO-+1N2O=>1NO2-+1N2	1.68E+10	0.0	0.0
279	NO2-+1O3=>1O2+1NO3-	5.40E+13	0.0	0.0
280	O-+1H2O+1N2=>H2O2-+N2	7.80E-05	0.0	0.0
281	O-+1H2O+1O2=>H2O2-+O2	7.80E-05	0.0	0.0
282	O2-+1H2O+1N2=>H2O3-+N2	1.32E-04	0.0	0.0
283	O2-+1H2O+1O2=>H2O3-+O2	1.32E-04	0.0	0.0
284	O3-+1H2O+1N2=>H2O4-+N2	1.62E-04	0.0	0.0
285	O3-+1H2O+1O2=>H2O4-+O2	1.62E-04	0.0	0.0
286	OH-+1H2O+1N2=>H3O2-+N2	1.50E-04	0.0	0.0
287	OH-+1H2O+1O2=>H3O2-+O2	1.50E-04	0.0	0.0
288	NO-+H2O+N2=>NO2H2-+N2	6.00E-05	0.0	0.0

Table 5 (continued): Reaction Mechanism, *A* units mol-cm-s-K, *E* units cal/mol

289	NO-+H2O+O2=>NO2H2-+O2	6.00E-05	0.0	0.0
290	NO2-+H2O+N2=>NO2H2O-+N2	9.60E-05	0.0	0.0
291	NO2-+H2O+O2=>NO2H2O-+O2	9.60E-05	0.0	0.0
292	H3O++1H2O2-=>2H2O+1OH	6.00E+17	0.0	0.0
293	H3O++1H2O3-=>2H2O+1HO2	6.00E+17	0.0	0.0
294	H3O++1H2O4-=>2H2O+OH+O2	6.00E+17	0.0	0.0
295	H3O++1H3O2-=>3H2O	6.00E+17	0.0	0.0
296	H3O++1NO2H2-=>2H2O+HNO	6.00E+17	0.0	0.0
297	H3O++1NO2H2O-=>2H2O+HNO2	6.00E+17	0.0	0.0
298	OH++1H2O2-=>1H2O+1HO2	6.00E+17	0.0	0.0
299	OH++1H2O3-=>H2O+OH+O2	6.00E+17	0.0	0.0
300	OH++1H2O4-=>H2O+HO2+O2	6.00E+17	0.0	0.0
301	OH++1H3O2-=>2H2O+O	6.00E+17	0.0	0.0
302	OH++1NO2H2-=>HNO2+H2O	6.00E+17	0.0	0.0
303	OH++1NO2H2O-=>HNO3+H2O	6.00E+17	0.0	0.0
304	O2++1H2O2-=>1H2O+1O3	6.00E+17	0.0	0.0
305	O2++1H2O3-=>1H2O+2O2	6.00E+17	0.0	0.0
306	O2++1H2O4-=>H2O+O3+O2	6.00E+17	0.0	0.0
307	O2++1H3O2-=>H2O2+HO2	6.00E+17	0.0	0.0
308	O2++NO2H2-=>H2O+NO3	6.00E+17	0.0	0.0
309	O2++NO2H2O-=>H2O+NO2+O2	6.00E+17	0.0	0.0
310	NO++1H2O2-=>1H2O+1NO2	6.00E+17	0.0	0.0
311	NO++1H2O3-=>1H2O+1NO3	6.00E+17	0.0	0.0
312	NO++1H2O4-=>H2O+NO2+O2	6.00E+17	0.0	0.0
313	NO++1H3O2-=>H2O+HNO2	6.00E+17	0.0	0.0
314	NO++1NO2H2-=>2NO+H2O	6.00E+17	0.0	0.0
315	NO++NO2H2O-=>NO2+NO+H2O	6.00E+17	0.0	0.0
316	O2-+NO+=>O2+N+O	6.00E+16	0.0	0.0
317	O3-+O+=>O3+O	1.20E+17	0.0	0.0
318	O3-+O2+=>O3+O2	1.20E+17	0.0	0.0
319	O3-+O2+=>2O+1O3	6.00E+16	0.0	0.0
320	O3-+NO+=>O3+1NO	1.20E+17	0.0	0.0
321	NO3-+NO+=>NO3+1N+1O	6.00E+16	0.0	0.0
322	NO3-+O2+=>NO3+O+O	6.00E+16	0.0	0.0
323	O-+O2+=>O+O2	1.20E+17	0.0	0.0
324	O-+O2++1O2=>O3+O2	1.20E+22	0.0	0.0
325	O-+NO++1O2=>NO2+O2	1.20E+22	0.0	0.0
326	O2-+O2+=>O2+O2	2.52E+17	0.0	0.0
327	O2-+NO++O2=>2O2+NO	1.20E+22	0.0	0.0

APPENDIX B: AIR ELECTRIC PROPERTIES

Air electric properties that were used in modeling are taken from [8].

Electron mobility:

$$\mu = 2 \cdot 10^{6} (0.1 \cdot \frac{E}{N})^{0.8} \quad cm^2 /(V \cdot s)$$

Diffusion of electrons (diffusion of ions is not taken into account):

$$D = 1800 \quad cm^2 / s$$

Ionization coefficient:

$$\alpha = N \cdot 1.4 \cdot 10^{-16} \exp(-\frac{660}{E / N}) \quad cm^{-1}$$

Electron positive ion recombination coefficient:

$$\beta = 5 \cdot 10^{-8} \quad cm^3 / s$$

Ion-ion recombination:

$$\beta = 2 \cdot 10^{-6} \quad cm^3 / s$$

APPENDIX C: FFT SOURCE CODE USED IN MULTI-STREAMER PATTERN ANALYSIS

Given source code uses FFTW library in order to calculate FFT [39].

```
/* Multi dim arrays row-based order (C-order)
      i  j
  in [X][Y] = in [j+Y*i]
    2 5 8 11
    1 4 7 10
    0 3 6  9
  in this code
  all arrays are in[Y][X] = in[ROW][COLUMN] = in [j][i] =
  in[i+j*RowSize]
  RowSize is number of Columns */
#include <windows.h>
#include <fftw.h>
#include <math.h>
#include "FRecord.h"
#include "resource.h"
#define filterSelectorAbout    0
#define filterSelectorParameters 1
#define filterSelectorPrepare  2
#define filterSelectorStart    3
#define filterSelectorContinue 4
#define filterSelectorFinish   5
#define userCanceledErr       (-128)
#define VER  "2.2"
fftw_complex *complex_in;
void Pump_FFTtoPowerSpectra(unsigned char* out, fftw_complex
*complex_in, int xsize, int ysize);
void Pump_FFTtoPowerSpectraNoShift(unsigned char* out,
fftw_complex *complex_in, int xsize, int ysize);
HANDLE hDllInstance = NULL;
BOOL APIENTRY DLLEntry(HANDLE hInstance, DWORD fdwReason, LPVOID
lpReserved)
```

```
{
      if (fdwReason == DLL_PROCESS_ATTACH)
            hDllInstance = hInstance;
      return 1;
}
short ErrorCode = 0;
int FAR PASCAL ProbaDialog (HWND hWnd, unsigned int wMsg,
unsigned int wParam,LONG lParam)
{
      switch( wMsg )
      {
            case WM_COMMAND:
                  switch(LOWORD(wParam))
                  {
                        case IDCANCEL:
                              ErrorCode =  userCanceledErr;
                              EndDialog( hWnd,0 );
                              break;
                        case IDOK:
                              EndDialog( hWnd,0 );
                              break;
                  }
      }
      return 0;
}
void ENTRYPOINT (const short  selector, FilterRecord   *fPB, long
*data, short *result)
{
      HWND HWnd=NULL;
      PlatformData *platform;
      if(selector==0) platform = (PlatformData *)(fPB-
>serialNumber);
            else platform = (PlatformData *)(fPB-
>platformData);
      if(platform!=NULL)HWnd = (HWND)platform->hwnd;

      if(selector == filterSelectorStart)
{
```

```
SetRectMy(&fPB->inRect  ,0,0,fPB->imageSize.h, fPB->imageSize.v);
SetRectMy(&fPB->outRect ,0,0,fPB->imageSize.h, fPB->imageSize.v);
SetRectMy(&fPB->maskRect,0,0,0,0);
                  fPB->inLoPlane    =0;
                  fPB->inHiPlane    =fPB->planes-1;
                  fPB->outLoPlane   =0;
                  fPB->outHiPlane   =fPB->planes-1;
      }
            if(selector == filterSelectorContinue)
            {
                        if(
DialogBox((HINSTANCE)hDllInstance,"proba",HWnd,ProbaDialog))
                        {
                              MessageBox(HWnd, "Can't load dialog
                        box!\n", NULL, MB_OK | MB_APPLMODAL );
                              ErrorCode = userCanceledErr;
                        }
                        return;}
            char string[80];
            char strCaption[] = {"Info"};
            SetRectMy(&fPB->inRect  ,0,0,0,0);
            SetRectMy(&fPB->outRect ,0,0,0,0);
            SetRectMy(&fPB->maskRect,0,0,0,0);
            unsigned char* buf1;
            unsigned char* in  = fPB->inData;
            unsigned char* out = fPB->outData;
            int xsize = fPB->imageSize.h; //Row Size
            int ysize = fPB->imageSize.v; //Col Size
            buf1 = new unsigned char [xsize*ysize];
sprintf(string, "FFT: Size_xy( %d %d) bpr (in out)= (%d %d) color %d
Ver: %s\n", xsize, ysize,fPB->inRowBytes, fPB->outRowBytes, fPB-
>planes, VER);
            MessageBox(HWnd, string, strCaption, MB_OK | MB_APPLMODAL
);
            fftwnd_plan p;
            int i, j;
            int nSum;
complex_in = (fftw_complex *) realloc(complex_in, xsize * ysize *
sizeof(fftw_complex));
            //buf1<=in
```

```
            for(i=0;i<xsize;i++)
            for(j=0;j<ysize;j++)
            {
                  nSum = 0;
                  for(long plane=0;plane<fPB->planes;plane++)
                  {
            nSum += in[fPB->inRowBytes*j + fPB->planes*i + plane];
                  }
                  nSum = nSum/fPB->planes;
                  buf1[xsize*j + i] = nSum;
            }
                  for(i=0;i<xsize;i++)
                  for(j=0;j<ysize;j++)
                  {
                        complex_in[xsize*j + i].im = 0;
                        complex_in[xsize*j + i].re = buf1[xsize*j + i];
                  }
p = fftw2d_create_plan(ysize, xsize, FFTW_FORWARD, FFTW_ESTIMATE |
FFTW_IN_PLACE);
            fftwnd_one(p, complex_in, NULL);
            fftwnd_destroy_plan(p);
            Pump_FFTtoPowerSpectra(buf1,complex_in, xsize, ysize);
            for(i=0;i<xsize;i++)
            for(j=0;j<ysize;j++)    {
                  for(long plane=0;plane<fPB->planes;plane++)
                  {
out[fPB->outRowBytes*j + fPB->planes*i + plane] = buf1[xsize*j + i];
                  }
            }
      delete [] buf1;
            SetRectMy(&fPB->inRect  ,0,0,0,0);
            SetRectMy(&fPB->outRect ,0,0,0,0);
            SetRectMy(&fPB->maskRect,0,0,0,0);
            } //if(selector == filterSelectorContinue)
      *result = 0;
       return;
      }
```

```
void Pump_FFTtoPowerSpectraNoShift(unsigned char* out, fftw_complex
*complex_in, int xsize, int ysize)
      {
            double * double_buf;
            double_buf = new double  [xsize*ysize];
            int i, j;
            int xcenter = xsize/2;
            int ycenter = ysize/2;
double dMax = log10(1+sqrt(complex_in[0].im*complex_in[0].im +
complex_in[0].re*complex_in[0].re));
double dMin = log10(1+sqrt(complex_in[0].im*complex_in[0].im +
complex_in[0].re*complex_in[0].re));
            double dDelta;
            for ( i = 0; i<xsize * ysize; i++)
            {
                  double_buf[i] =
log10(1+sqrt(complex_in[i].im*complex_in[i].im +
complex_in[i].re*complex_in[i].re));
                  if (double_buf[i]<dMin) dMin = double_buf[i];
                  if (double_buf[i]>dMax) dMax = double_buf[i];
            }
            dDelta = dMax-dMin;
            if (dDelta==0)
            {
                  delete [] double_buf;
                  double_buf = 0;
                  return;
            }
            for ( i = 0; i<xsize * ysize; i++)
            out[i] = unsigned char( 255*(double_buf[i]-dMin)/dDelta);
            delete [] double_buf;
            double_buf = 0;
      }
void Pump_FFTtoPowerSpectra(unsigned char* out, fftw_complex
*complex_in, int xsize, int ysize)
      {
            double * double_buf = 0;
            double_buf = new double  [xsize*ysize];
            int i, j;
```

```
            int xcenter = xsize/2;
            int ycenter = ysize/2;
double dMax = log10(1+sqrt(complex_in[0].im*complex_in[0].im +
complex_in[0].re*complex_in[0].re));
double dMin = log10(1+sqrt(complex_in[0].im*complex_in[0].im +
complex_in[0].re*complex_in[0].re));
            double dDelta;
            for ( i = 0; i<xsize * ysize; i++)
            {
double_buf[i] = log10(1+sqrt(complex_in[i].im*complex_in[i].im +
complex_in[i].re*complex_in[i].re));
                  if (double_buf[i]<dMin) dMin = double_buf[i];
                  if (double_buf[i]>dMax) dMax = double_buf[i];
            }
            dDelta = dMax-dMin;
            if (dDelta==0)
            {
                  delete [] double_buf;
                  double_buf = 0;
                  return;
            }
            /* 2 1
               3 4 */
            //2 -> 4
            for ( i = 0; i<xcenter; i++)
            for ( j = 0; j<ycenter; j++)
            {
out[(i+xcenter)+(j+ycenter)*xsize] = unsigned char(
255*(double_buf[i+j*xsize]-dMin)/dDelta);
            }
            // 1 -> 3
            for ( i = xcenter; i<xsize; i++)
            for ( j = 0; j<ycenter; j++)
            {
out[(i-xcenter)+(j+ycenter)*xsize] = unsigned char(
255*(double_buf[i+j*xsize]-dMin)/dDelta);
            }
            // 3 -> 1
            for ( i = 0; i<xcenter; i++)
```

```
            for ( j = ycenter; j<ysize; j++)
            {
out[(i+xcenter)+(j-ycenter)*xsize] = unsigned char(
255*(double_buf[i+j*xsize]-dMin)/dDelta);
            }
            // 4 -> 2
            for ( i = xcenter; i<xsize; i++)
            for ( j = ycenter; j<ysize; j++)
            {
out[(i-xcenter)+(j-ycenter)*xsize] = unsigned char(
255*(double_buf[i+j*xsize]-dMin)/dDelta);
            }
            delete [] double_buf;
            double_buf = 0;
      }
```

APPENDIX D: MATLAB SCRIPT FOR VORONOI POLYHEDRA CONSTRUCTION AND ANALYSIS

```
%dbd = imread(' Experimental image file name ); %expr
%dbd = imread(' Simulation image file name'); %simulation
figure, imshow(dbd), title('dbd surface data');
se = strel('disk', 5);
Itop = imtophat(dbd, se);
Ibot = imbothat(dbd, se);
figure, imshow(Itop, []), title('top-hat image');
figure, imshow(Ibot, []), title('bottom-hat image');
Ienhance = imsubtract(imadd(Itop, dbd), Ibot);
figure, imshow(Ienhance), title('original + top-hat - bottom-
hat');
Iec = imcomplement(Ienhance);
%Iec = Ienhance;
figure, imshow(Iec), title('complement of enhanced image');
Iemin = imextendedmin(Iec, 210);
figure, imshow(Iemin), title(' extended  minima image');
%these two lines good for experemental data not for simulated one
Iemin = imdilate(Iemin, strel('square', 3));
Iemin = medfilt2(Iemin);
figure, imshow(Iemin), title('eroded minima image');
%look for black regions
wat = watershed(Iemin);
rgb = label2rgb(wat);
figure, imshow(rgb);
title('watershed segmented image');
%extracting information
size = max(wat(:));
fprintf('Number of sites %d\n', size);
stats = regionprops(wat, 'Area', 'Orientation', 'Centroid');
area   = [stats.Area];
orient = [stats.Orientation];
center = [stats.Centroid];
```

```
center = reshape(center, 2, size);

figure, plot(center(1,:), center(2,:) , '.'),title('Extracted
positions');
figure, hist(area), title('watershed area distr');
figure, plot(area, orient, '.');
title('Relationship of Particle Orientation to Area');
xlabel('particle area (pixels)');
ylabel('particle orientation (degrees)');
%convexhull
xp = center(1,:);
yp = center(2,:);
K = convhull(xp,yp); plot(xp(K),yp(K),'r-',xp,yp,'b+')
%IN = inpolygon(xp,yp,xp(K),yp(K));
%voronoi polyhedra
figure, plot(center(1,:), center(2,:) , '.')
[v,c]=voronoin(center' );
for i = 1:length(c)
if all(c{i}~=1)   % If at least one of the indices is 1,
                  % then it is an open region and we can't
                  % patch that.
if (inpolygon(v(c{i},1), v(c{i},2),xp(K),yp(K)))>0 %vertex inside
convexhull
patch(v(c{i},1),v(c{i},2), length(c{i})); % use color i.
vor_area(i)      = polyarea(v(c{i},1),v(c{i},2));
vor_perimeter(i) = poly_perimeter(v(c{i},1),v(c{i},2));
vor_cdist(i)     = 4*pi*vor_area(i)/(vor_perimeter(i)^2);
vor_angl(i)      = length(c{i});
end
end
end
axis equal,colormap jet,  colorbar
%distribution plot
figure, hist(vor_area), title('voronoi area distr');
figure, hist(vor_angl, [3 4 5 6 7 8 9 10]), title('voronoi angle
distr');
figure, hist(vor_perimeter), title('voronoi perimeter distr');
```

```
figure, hist(vor_cdist), title('voronoi cdist distr');

vor_area = vor_area';
vor_perimeter = vor_perimeter';
vor_cdist = vor_cdist';
vor_angl = vor_angl';
idx = find([stats.Area] > 100);
BW2 = ismember(wat,idx);
figure, imshow(BW2);
clear;
function perimeter = poly_perimeter(x,y)
siz = length(x);
per = 0;
for i = 1:1:siz-1
per = per + sqrt( (x(i)-x(i+1)).^2 + (y(i)-y(i+1)).^2 )
end;
per = per + sqrt( (x(1)-x(siz)).^2 + (y(1)-y(siz)).^2 );
perimeter = per
```